

Exoplanet Transit Candidate Identification in TESS Full-Frame Images via a Transformer-Based Algorithm

Helem Salinas^{1,2*}, Rafael Brahm^{4,5,6}, Greg Olmschenk^{3,7} †, Richard K. Barry³ ‡, Karim Pichara^{1,5}, Stela Ishitani Silva^{3,8} §, Vladimir Araujo⁹

¹Departamento de Ciencias de la Computación, Facultad de Ingeniería, Pontificia Universidad Católica de Chile, Santiago 7820436, Chile

²Department of Physics, The Catholic University of America, Washington, DC 20064, USA

³NASA Goddard Space Flight Center, Greenbelt, MD 20771, USA

⁴Facultad de Ingeniería y Ciencias, Universidad Adolfo Ibáñez, Av. Diagonal Las Torres 2640, Peñalolén, Santiago, Chile

⁵Millennium Institute for Astrophysics, Av. Vicuña Mackenna 4860, 782-0436 Macul, Santiago, Chile

⁶Data Observatory Foundation, Chile

⁷Department of Astronomy, University of Maryland, College Park, MD 20742, USA

⁸Oak Ridge Associated Universities, Oak Ridge, TN 37830, USA

⁹Department of Computer Science, KU Leuven, Celestijnenlaan 200A, B-3001 Leuven, Belgium

12 February 2025

ABSTRACT

The Transiting Exoplanet Survey Satellite (TESS) is surveying a large fraction of the sky, generating a vast database of photometric time series data that requires thorough analysis to identify exoplanetary transit signals. Automated learning approaches have been successfully applied to identify transit signals. However, most existing methods focus on the classification and validation of candidates, while few efforts have explored new techniques for the search of candidates. To search for new exoplanet transit candidates, we propose an approach to identify exoplanet transit signals without the need for phase folding or assuming periodicity in the transit signals, such as those observed in multi-transit light curves. To achieve this, we implement a new neural network inspired by Transformers to directly process Full Frame Image (FFI) light curves to detect exoplanet transits. Transformers, originally developed for natural language processing, have recently demonstrated significant success in capturing long-range dependencies compared to previous approaches focused on sequential data. This ability allows us to employ multi-head self-attention to identify exoplanet transit signals directly from the complete light curves, combined with background and centroid time series, without requiring prior transit parameters. The network is trained to learn characteristics of the transit signal, like the dip shape, which helps distinguish planetary transits from other variability sources. Our model successfully identified 214 new planetary system candidates, including 122 multi-transit light curves, 88 single-transit and 4 multi-planet systems from TESS sectors 1-26 with a radius $> 0.27 R_{\text{Jupiter}}$, demonstrating its ability to detect transits regardless of their periodicity.

Key words: methods: data analysis, planets and satellites: detection

1 INTRODUCTION

The amount of astronomical data collected from both space and ground-based telescopes has increased rapidly. Given the vast amount of data, the task of analysis and examination becomes quite costly and is also prone to human error. Process automation plays an important role in helping to improve the efficiency and accuracy of detection and classification.

During the last decade, more than a million stars have been observed in the search for transiting exoplanets. Among the most no-

table contributors is NASA’s Kepler space telescope, launched in 2009 (Borucki et al. 2010). Kepler has identified nearly 4,000 potential planet candidates, of which approximately 2,700 have been confirmed as exoplanets to date. Kepler’s successor, NASA’s Transiting Exoplanet Survey Satellite (TESS; Ricker et al. 2014) was launched in April 2018 and is currently monitoring most of the sky searching for transiting exoplanet candidates. To date, TESS has discovered 561 confirmed exoplanets and identified thousands of additional planet candidates, significantly expanding our understanding of planetary systems beyond our solar system. TESS monitors millions of stars across approximately 90% of the sky, emphasizing the detection of exoplanets around nearby and bright stars. TESS observes each sector for ~ 27 days before reorienting to observe the next sector. The data products produced by the TESS mission include two types

* E-mail: yhsalinas@uc.cl

† ORCID: 0000-0001-8472-2219

‡ ORCID: 0000-0003-4916-0892

§ ORCID: 0000-0003-2267-1246

of data: small summed image subarrays (“postage stamps”) centred on pre-selected targets, also known as target pixel files (TPFs), and summed full-frame images (FFIs), which capture collections of pixels observed simultaneously (Guerrero et al. 2021). From these data products, the primary goal of TESS is to discover hundreds of transiting planets smaller than Neptune, including dozens comparable in size to Earth (Ricker et al. 2015).

The current standardized identification process of transiting exoplanet candidates from photometric time series involves two main steps. First, long-term flux variations are removed, and periodic transit-like signals are identified by phase-folding the light curve to different orbital periods, times of transit and transit duration (e.g. Tenenbaum et al. 2012). This process yields Threshold Crossing Events (TCEs), which include both potential exoplanets and false positives like eclipsing binaries and instrumental artifacts. The second step involves vetting TCEs by rejecting false positives based on the properties of the phase-folded transiting light curves, stellar properties, and follow-up observations. Typically, experts manually examine possible exoplanet transit signals, a labour-intensive process prone to human error and increasingly demanding due to large data volumes. To address this, several efforts have been made to automate the classification of light curves.

Meanwhile, with the advent of Deep Learning (DL) LeCun et al. (2015), neural network (NN) architectures have revolutionized numerous fields of scientific research, leading to substantial advancements in image processing, classification, facial recognition, voice recognition, and Natural Language Processing (NLP; Krizhevsky et al. 2017; Ciregan et al. 2012; He et al. 2016; Voulodimos et al. 2018; Vaswani et al. 2017). DL techniques, particularly convolutional neural networks (CNN; Krizhevsky et al. 2012), have been notably applied to classification tasks, where classification in machine learning refers to the task of predicting the class to which the input data belongs. In particular, it was used to classify transit signals for the validation of exoplanet candidates and has also been applied in the transit search process, though to a smaller extent. In the field of exoplanet transit signal classification, 1D CNNs have been commonly used (e.g. Osborn et al. 2020; Rao et al. 2021; Tey et al. 2023). Specifically, the approaches focus on validating transit signals obtained through phase-folding light curves, which depend on prior transit parameters such as period, duration and depth derived from initial detection processes. These methods utilize both local and global views of folded light curves for distinguishing exoplanet transits from false positives, but they do not perform the initial transit search or parameter extraction themselves. Regarding the search for new exoplanet candidates, Olmschenk et al. (2021) developed a pipeline for detecting and vetting periodic transiting exoplanets. Their approach utilizes the TESS FFIs light curves and employs a 1D-CNN for candidate identification. Another approach, as demonstrated by Cui et al. (2021), employs a 2D object detection algorithm based on YOLOv3 network (Redmon & Farhadi 2018), which was trained on Kepler data to detect exoplanet signals.

As mentioned above, proposed DL pipelines have primarily focused on classifying transiting exoplanet signals, where transit detections are confirmed by aligning several repeated transits with the orbital period, resulting in enhanced signal detection. In contrast, few efforts have explored new techniques for discovering candidates without requiring prior transit parameters. Consequently, while current standardized pipelines for detecting transiting exoplanets have reached a high level of efficiency, they have at least two important limitations, namely: i) they require de-trending processes to remove long-term flux variations of stellar origin, which could vary the trend of the sequence, introduce artifacts into the light curve, or remove

exoplanet transits; and ii) they rely on the periodicity of the transit signal in the light curve. These pipelines could be therefore missing exoplanets that present strong transit timing variations (TTV) and/or those that present just one transit in the light curve (single transitters).

Regarding single transitters, many signals in observed light curves arise from stochastic processes—whether instrumental or astrophysical—which can often mimic single transit events (Foreman-Mackey et al. 2016). To accurately determine the orbital period of this single transit, detecting additional transits in multiple sectors is necessary, given that interruptions in the light curves typically require at least three transit events to reliably constrain the orbital period. This is because the presence of a single transit event does not provide sufficient information to confirm the periodic nature of the signal. This leads to considerable challenges that hinder a search for single transit events. For instance, the transit probability for long-period planets could be lower, particularly for those with orbital periods that exceed the duration of continuous observations (Hawthorn et al. 2024). This is also due to the fact that transit probability P_{tr} is proportional to r_*/a and for long-period planets, the semi-major axis a is larger, resulting in a lower P_{tr} . Despite the challenges associated with detecting single transitters, a small number of named “monotransitters” have been confirmed, where a single transit-like feature appears in the light curve but does not repeat (Gill et al. 2020a,b; Lendl et al. 2020).

Due to observational biases, the vast majority of well-characterized transiting giant planets have orbital periods shorter than 10 days [e.g.] (Hartman et al. 2019; Magliano et al. 2023). The existence of these planets, known as hot Jupiters, has challenged theories regarding the formation and evolution of giant planets in general (Pollack et al. 1996). To solve these open questions, it is crucial to discover and characterize giant planets with longer periods (warm Jupiters) that are not extremely irradiated by their host stars, and their physical and orbital properties can be compared to outcomes of different formation and migration processes (Dawson & Johnson 2018). While TESS has significantly increased the sample of well-characterized transiting warm Jupiters (e.g. Dawson et al. 2021; Grieves et al. 2022; Brahm et al. 2023; Battley et al. 2024), an important fraction of them might still be undiscovered because they are presented as single transitters in TESS data (e.g. Gill et al. 2020c).

In this work, we propose an approach to identify exoplanet transit signals within a light curve without requiring prior transit parameters. This enables us to discover new exoplanet candidates directly from the complete light curve, avoiding the initial dependence on traditional techniques that phase-fold the light curve to identify periodic transit-like signals. We propose an architecture based on a sequential model inspired by the Transformer (Vaswani et al. 2017). This type of architecture has demonstrated its effectiveness in handling complex scenarios, outperforming other model types such as recurrent neural networks (RNN; Cho et al. 2014) and CNNs, in particular for sequential data (Hawkins 2004; Lakew et al. 2018; Karita et al. 2019). Our architecture learns the characteristics of a planetary transit signal, regardless of whether the signal is periodic throughout the light curve. While instrumental systematics are typically removed during preprocessing, to compute light curves, stellar-origin variations remain in the data. Our NN is therefore exposed to both long-term and short-term stellar variability, including activity-related fluctuations on timescales of days. Specifically, the architecture is designed to identify and differentiate between transit signals and the variability of stars. This type of architecture has been explored and applied by Salinas et al. (2023) for classifying exoplanet transit signals and distinguishing them from false positives, and our NN extends this approach to the search for new exoplanet candidates. In particular,

our architecture is designed to make predictions directly from the light curve. The NN captures temporal patterns and long-range dependencies within light curves without depending on prior transit parameters, such as transit depth, transit period and transit duration. This independence from periodicity allows our NN to detect both multi-transit and single-transit signals, making it particularly effective for identifying single transits that have often been missed by previous approaches focused primarily on light curves with multiple transits of the same planet.

This article is organized as follows: Section 2 introduces the key concepts that inspired this work, where we briefly describe the Transformer encoder related to the original architecture (Vaswani et al. 2017) in order to understand our proposal for exoplanet transit signal identification. Section 3 describes the photometric data used in our work. Section 4 explains the proposed methodology in detail, including the NN training process. The model analysis and results are described in Section 5. In Section 6, we describe the exoplanet candidates found. Finally, in Section 7 we present overall conclusions and future work.

2 BACKGROUND THEORY OF TRANSFORMER ENCODER

Recent developments in DL have introduced new approaches to processing sequential data. Among these, the Transformer model proposed by Vaswani et al. (2017) has recently demonstrated significant success in capturing long-range dependencies compared to previous approaches focused on sequential data (Hawkins 2004; Lakew et al. 2018; Karita et al. 2019). Initially developed for Natural Language Processing, it has since been adapted to various domains, including time-series analysis. In NLP, data typically consists of discrete tokens, such as words or characters, arranged in a sequence to form sentences or documents. In astronomy, by contrast, the data often comes in the form of continuous measurements, such as light curves that represent stellar brightness over time. (In the present time-series context, for example, the term range refers to the length of the time baseline between separate elements within the data.) Both are sequential data, where the order of elements within the sequence is essential to uncovering patterns and relationships.

The original Transformer model consists of an encoder and a decoder (Vaswani et al. 2017). In this work, we focus on the encoder. The encoder processes the input sequence to generate a representation, which captures the essential patterns and features of the data.

The core of the Transformer encoder is a mechanism called self-attention, which builds upon the original attention mechanism proposed by Bahdanau et al. (2014). Self-attention enables the NN to “attend” to all parts of the input sequence simultaneously. This mechanism allows the NN to evaluate the importance of each element in the sequence in relation to every other element, weighing how much each data point should contribute to the final representation. It enables the NN to capture both local and long-range dependencies. Unlike traditional methods that focus on short-range dependencies, self-attention allows the Transformer to understand the full temporal structure of the data (Lakew et al. 2018; Karita et al. 2019).

Figure 1 shows the core of the Transformer encoder, and provides a detailed view of the self-attention mechanism. The input sequence is represented as a series of data points, denoted as (x_1, x_2, \dots, x_n) , where n is the length of the sequence. This input is first encoded into a continuous vector space through the embedding layer, and each x_i is represented as a vector $x_{\text{emb}_i} \in \mathbb{R}^d$, where d is the embedding dimension. Vector embedding is a way to represent data symbols (such as

words, observations, or images) in a continuous, transformed space. Embeddings can be numeric representations or generated through NNs. As shown in Figure 1(a), this representation is then combined with a positional encoding, which incorporates information about the order of the data points, capturing their relationships in the temporal dimension (Vaswani et al. 2017), such as patterns and relationships that depend on the temporal order of the data, such as periodic trends or sequential dependencies. The positional encoding is essential because the Transformer architecture, unlike RNN or CNN, does not have an inherent way to understand the order of elements in a sequence (Gehring et al. 2017). This combined representation is then passed to the encoder. Within the encoder, the self-attention mechanism captures both local and global dependencies, enabling the extraction of complex features and patterns.

The self-attention mechanism used within the encoder to process the input sequence, in this case a light curve. The self-attention process involves three components: queries Q , keys K and values V . As shown in Figure 1(b), each element in the sequence generates a query, which asks how much attention it should pay to the other elements. The query is compared to keys, which represent the context, and an attention score is calculated. The score is calculated using the scaled dot-product of Q and the transpose of K . These values are then passed through a softmax function to convert the values into a probability distribution that sums to 1, while sharpening the distribution. This score determines how much focus each element should give to others.

Finally, V , weighted by the attention scores, are then combined to produce the final output of the self-attention feature map. This feature map encapsulates the relationships across the sequence and contributes to the encoded representation z . In the case of multihead self-attention (MSA), multiple attention mechanisms are applied in parallel, capturing different aspects of the relationships across the sequence (see the Appendix A for more details). The decoder then uses this encoded representation z to produce outputs such as probability estimates for the presence of planetary transit signals into a light curve. This approach enables the model to detect exoplanet transit signals directly from the complete light curve without prior transit parameters even if only one transit is exhibited during the entire observation sequence.

Transformers have shown significant potential for encoding time series data in astronomy (e.g. Allam Jr & McEwen 2021; Zerveas et al. 2021; Morvan et al. 2022). In the field of exoplanet science, Salinas et al. (2023) implemented a Transformer model specifically tailored to distinguish exoplanet transit signals from false positives, highlighting the capability of the architecture to identify and interpret the characteristics of exoplanet signals. In the context of exoplanet transit signal detection, the ability of the Transformer to model long-range dependencies is highly beneficial, as it can identify signal patterns associated with stellar variability that might otherwise be mistaken for false positives. This allows the model to accurately distinguish true planetary transits within the entire light curve, even amid the variability of the stars.

3 TESS DATA

For the present work, we have used light curve data obtained from the Mikulski Archive for Space Telescopes (MAST). The light curves are extracted from the TESS full-frame images (FFIs), which were captured at a cadence of 30 minutes during its primary mission. The time stamps for these measurements are given in Barycentric TESS Julian Date (BTJD) format, which is specific to the TESS

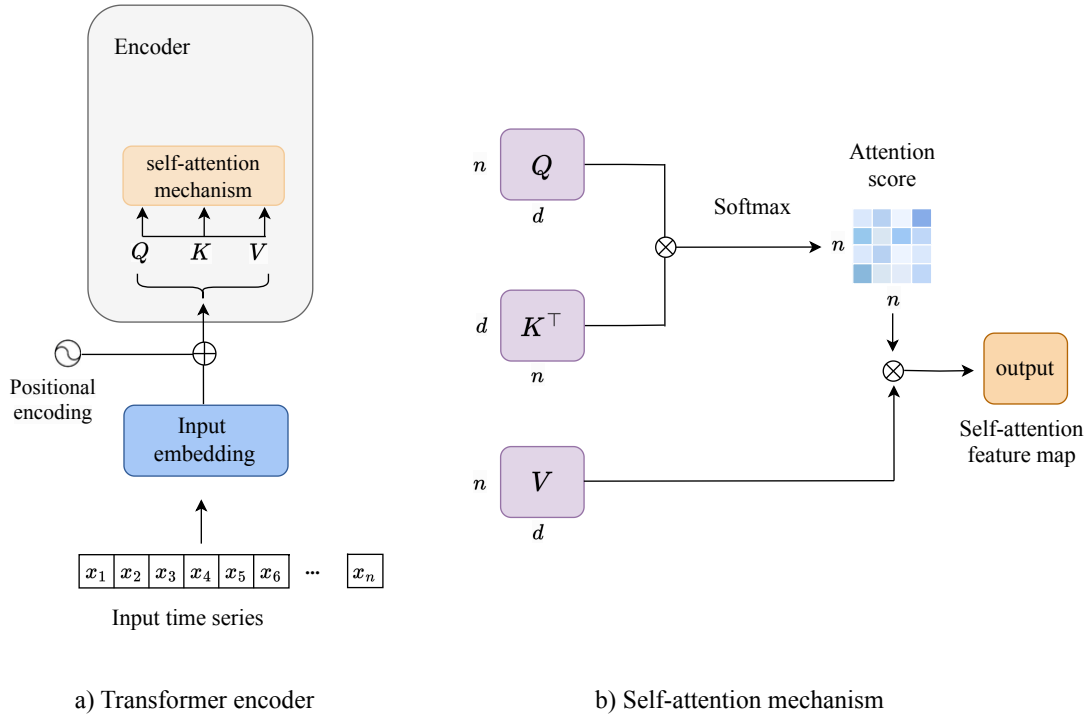


Figure 1. (a) the transformer encoder, which processes time series inputs using positional encodings combined with input embeddings, and computes feature representations through a self-attention mechanism. (b) explains the self-attention mechanism, where the Q , K matrices are used to calculate attention scores. These scores are then applied to the V to produce the self-attention feature map.

mission. BTJD is defined as $BTJD = BJD - 2457000.0$ days, where BJD refers to the Barycentric Julian Date. The use of BTJD ensures precise timing by taking into account the motion of Earth and other relativistic effects. To obtain the light curves, we use the outputs of the TESS Science Processing Operations Center (SPOC) pipeline (Caldwell et al. 2020) (see Section 3.1). SPOC pipeline processes the data of targets selected from the FFIs to create target pixel and light curve files for up to 150,000 targets per sector. By selecting a specific set of target stars from these FFIs, SPOC generates the same outputs as for the pre-selected 2-min cadence targets, including calibrated target pixel files and simple aperture photometry (SAP) flux.

3.1 TESS-SPOC FFI light curves

For the primary mission of TESS, the FFIs are captured at a 30-minute cadence and are crucial for large-scale surveys, enabling the simultaneous monitoring of thousands of stars. To optimize the utility of FFI data, SPOC employs a selection process that prioritizes targets based mainly on their crowding metric (Bryson et al. 2020) and brightness. Specifically, targets with a crowding metric of ≥ 0.5 are selected, ensuring that at least 50% of the flux within the photometric aperture originates from the target star itself. Additionally, SPOC focuses on TESS Input Catalog (TIC) objects with TESS magnitudes of $T \leq 16$, balancing the need for both bright and isolated targets to maximize the scientific return from the FFI data (Caldwell et al. 2020). Building on this, our architecture is trained with the light curves processed by SPOC from TESS sectors 1-26. Each sector was

observed continuously for about 27 days, with FFIs captured at a 30-minute cadence.

The light curves computed by SPOC from the FFIs include the stellar flux (PDCSAP_FLUX), which has been corrected for instrumental systematics and shows fewer systematic trends. In addition to the flux, SPOC also provides detailed information on the centroid position of the target star and the background flux. The centroids are a time series that represents the pixel position of the centre of the light, which varies throughout the observation. This information allows us to determine the location of the transit within the pixels. When the centroid shifts during a transit event, we can identify whether the observed flux variations are coming from the target star or from nearby sources. The background time series represents the estimated flux contribution from nearby sources, such as nearby stars or unresolved objects, to the target aperture. It is derived from pixels located outside the photometric aperture but within the same CCD frame. This estimation aims to minimize the influence of nearby stars, though it is not always possible to completely exclude their effect, but their contribution is minimized. Both time series allow the distinction between true transits and other astrophysical phenomena that might affect the measured light curve caused by background contamination or blended stellar sources. We use these data sets; PDCSAP_FLUX, centroids, and background time series as inputs to our architecture, enhancing the accuracy and reliability of exoplanet transit detection.

4 METHODOLOGY

In this section, we describe our methodology, which is designed to determine the confidence level of potential transiting exoplanets within a given FFI light curve. Our work is mainly motivated by the need to detect exoplanet candidates observed by the TESS mission. To determine the confidence level, our proposed architecture considers the flux, centroid, and background time series as input of our NN. Our methodology consists of three main steps, which we describe in this section. First, in Section 4.1, we detail the data preprocessing steps used to construct our input representation, such as the time series and the data augmentation techniques employed. Section 4.2 discusses the ground truth data utilized in our analysis. Finally, Section 4.3 presents the design of our proposed NN architecture, with a description of the experimental setup and training details.

4.1 Data preprocessing

The preprocessing of the light curves provided by SPOC prepares them for model input through necessary transformations. In this process, we ensure that the time series are in a consistent format, allowing the NN to process and detect significant patterns within the light curves.

4.1.1 Flux, centroid, and background time series

Each light curve is processed to obtain a uniform length of 1000 data points, reflecting the approximate median length of single-sector light curves derived from TESS FFI data. Light curves longer than 1000 data points are truncated to this length. And, for light curves with fewer data points, we extend them by repeating the initial segment until they reach 1000 points. This standardization allows the same sequence sizes for the input for our model. Following length adjustment, we normalize the flux time series values. Specifically, we subtract the mean and divide by the standard deviation, and these values are linearly transformed to a range of -1 to 1.

We also incorporate two more time series. First, we included the centroid information into our input. For this, we use the CCD row and column positions of the target centroid provided in the SPOC dataset, with x_{row} representing the row position and y_{col} representing the position of the column. To characterize the centroid displacement, we compute its absolute magnitude as $r_{\text{centroid}} = \sqrt{x_{\text{row}}^2 + y_{\text{col}}^2}$. Then, the centroid time series is then normalized to the range -1 to 1, following the same procedure as the flux. Finally, we include background time series from the light curves, which is also normalized in the same way as the flux and centroid time series. This ensures that the background data, along with flux and centroid information, are on a comparable scale to maintain consistency across all input features.

4.1.2 Augmentation of training data

Through various augmentation methods, the NN is allowed to learn more generalized features and prevent network overfitting. We applied four techniques, exclusively to the training dataset. First, we add white noise to the flux values with a standard deviation randomly chosen from a uniform distribution between 0 and the mean of the flux. Second, we use random roll augmentation, which cyclically shifts the time series data for flux, centroid, and background by a random number of positions. This shift generates variations in the data without altering the core characteristics of the signal, thus preventing the model from overfitting to specific patterns. Third, we apply random

split and swap augmentation, where the time series data is split at a random index, and the resulting segments are swapped, maintaining temporal relationships while generating new variations. As fourth and last, mirror augmentation is used, which involves flipping the time series data along the time dimension. By reversing the order of data points, this technique creates a mirrored version of the original series, introducing further variations while preserving the overall patterns and relationships within the data.

As mentioned before, these augmentation methods are specifically applied to the training data and not to the validation or test datasets, ensuring that the model performance evaluation remains unbiased and reflective of its generalization capabilities. Specifically, the augmentation technique applied to each sample is randomly selected in every iteration, meaning that the model always sees different variations of the data. The stochastic nature of this augmentation strategy allows the model to be exposed to varying patterns and conditions, making it less likely that the model will memorize specific patterns present in the training data. This approach not only broadens the range of scenarios the model is trained on but also significantly enhances its robustness and ability to generalize to new, unseen data (Shorten & Khoshgoftaar 2019). This helps the model to perform optimally during the inference phase.

4.2 Ground truth data set

For our ground truth dataset, we collected samples for both positive and negative cases. We categorized the collected labels into three primary sets of light curves: known transiting planets, eclipsing binaries (EBs), and non-transit signals. The first set, representing positive cases, was drawn from the TESS Exoplanet Follow-up Program (ExoFOP-TESS) catalog¹, which provided labels for light curves corresponding to confirmed and known planets. This dataset was utilized for training, validation, and testing of our NN. It is important to mention that we excluded any unconfirmed planet candidates listed by ExoFOP-TESS, as many of these are later identified as false positives during follow-up observations.

The second set consisted of EBs collected from three main catalogues. First, we used the catalogue from Prša et al. (2022), which provides a collection of EBs observed by TESS. Second, we incorporated false positives classified as EBs from the ExoFOP-TESS catalogue. These targets were initially identified as planetary candidates but were later reclassified as EBs following detailed follow-up observations. Finally, we added a catalogue based on ML predictions from Yu et al. (2019) (referred as ML:Y19 in Table 1), which includes labelled EBs and is publicly available². EB contamination are among the most common false positives due to their periodic patterns, which are similar to true exoplanet transits. These strong negative cases were crucial for training the model to distinguish between true transits and false positives.

The third set consists of non-transit signals derived from a catalogue based on machine learning predictions from Yu et al. (2019). This dataset included labels for instrumental systematics (IS), stellar variability (V), and a Junk (J) class, which represents a mix of IS and V signals. With these non-transit light curves, we expanded the variety of negative cases. In addition, we included light curves labelled as false positives (FP) by the ExoFOP-TESS catalogue, ensuring that the selected false positives were not associated with EBs.

Since each target may have been observed in multiple sectors, and

¹ <https://exofop.ipac.caltech.edu/teess/>

² Available at <https://github.com/yuliang419/Astronet-Triage>

Table 1. Labels and datasets used to train and evaluate our model.

Label	Target	Catalogue	Total sectors 1-26
Positive	confirmed planet	ExoFOP	1230
Negative	EBs	TESS-EBs	9333
		ExoFOP	1049
		ML:Y19	6550
	Non-transit	ExoFOP	934
		ML:Y19	26200

exoplanet transits appear in specific sectors based on their periodicity, we filtered the light curves to include only those that captured the exoplanet transits. The same approach was applied to EBs, where we selected the light curves containing EB transits. This approach has the advantage of capturing the unique noise characteristics from each sector, as each sector introduces its own variations, which help train the model to recognize signals under different observational conditions. Table 1 provides a detailed summary of the light curves collected for each target.

Additionally, we trained our network using light curves artificially injected, following a process inspired by [Olmschenk et al. \(2021\)](#). We injected signals from one light curve into another, selected from the three primary sets of light curves described above. This involved injecting light curves containing transit signals from confirmed exoplanets into non-transit light curves. This approach allows the network to learn from a variety of signals, incorporating real stellar variability and noise conditions. To achieve this, we randomly selected a light curve from the base set and normalized it by applying a median scaling to produce a relative magnification signal. Next, we randomly sampled a non-transit light curve and scaled its values by the previously generated relative magnification signal. We repeated this process, injecting light curves from EBs into non-transit light curves. Thus, light curves injected with known or confirmed exoplanet signals were labelled as positive ground truth, while those injected with EBs signals were labeled as negative ground truth. Non-transit light curves remained as negative ground truth, ensuring they continued to represent non-planetary signals.

Our training setup involves showing the network three types of light curves in each iteration. Specifically, we ensured that each batch contained an equal number of light curves from planets, EBs, and non-transit signals. This balanced distribution forces the network to learn and differentiate between exoplanet transit signals, EB signals, and other false positives, improving its ability to distinguish each type of signal.

The ground truth dataset was divided into training, validation, and testing subsets. Specifically, 80% of the dataset was designated for training, 10% for validation, and 10% for testing. The testing subset provides a final assessment to measure the model’s generalization capabilities across different light curves and transit signals.

4.3 Neural network architecture

Our proposed architecture is illustrated in Figure 2, which integrates convolutional embeddings with a Transformer encoder to process

light curve data. The process begins with convolutional embedding, which operates on raw inputs such as flux, centroid, and background, extracting local features through localized patterns in the data. These embeddings are then combined with positional encodings, which inject information about the positions of data points in the sequence. Since transformer-based NN do not inherently process sequential information, positional encodings help the model understand the order of the data, enabling it to capture temporal dependencies and the relative positioning of data points ([Vaswani et al. 2017](#)). The combined sequence of embeddings is then passed into the Transformer encoder. Then, the transformer encoder outputs are passed through average pooling to condense the information, followed by a multi-layer perceptron (MLP) head, which maps the features into a classification space. This final stage produces the probability of the input light curve representing a light curve with exoplanet transit (class 1) or a light curve without exoplanet transit (class 0). The combination of convolutional embeddings for local feature extraction and Transformer encoders for global contextualization enables the model to robustly identify exoplanet signals, even when faced with complex stellar variability.

4.3.1 Tokens and convolutional embedding

The input time series data, including flux, centroid, and background, are first segmented into tokens, representing key features within the series. The first step for each piece of information is to generate an input sequence, for this, we generate a sequence of observations in terms of the flux, centroid and background time series, represented as $\{(x_1, c_1, b_1), (x_2, c_2, b_2), (x_3, c_3, b_3), \dots, (x_n, c_n, b_n)\}$, where x_i, c_i, b_i denote the flux, centroid, and background values, respectively, at each time step i . Here, n is the length of time steps in the sequence. Each concatenated vector is defined as:

$$x'_i = (x_i, c_i, b_i) \quad (1)$$

where $x' \in \mathbb{R}^m$, and m is the number of variables of our time series. After concatenation, the sequence of these concatenated vectors $X = \{x'_1, x'_2, \dots, x'_n\}$ is the input for the convolutional operation.

As second step, we build the model’s vector embeddings. To obtain this embedding, we apply two layers of 1D convolution to our input sequence X . Each resulting embedding vector, or token, captures essential information about the input signal. Figure 3 shows this embedding process, where each input element is processed by CNN kernels that slide across the time series, transforming each local window into a token. These tokens extract and capture local patterns and short-term dependencies within the convolution window to identify patterns of exoplanet transit signals. In this context, the CNN focuses on the time variations in brightness that occur over short intervals, allowing the model to detect the distinct shape of the exoplanet transit signal as it passes in front of its host star.

We denote the convolution filter coefficients as $\mathbf{w} \in \mathbb{R}^{n \times k}$, and the output of the convolution operation at position i is the embedding token v'_i which is computed as:

$$v'_i = \mathbf{w}_i^{(k)} \cdot x'_i = \mathbf{w}_i^{(k)} \cdot (x_i, c_i, b_i) \quad (2)$$

In the first CNN layer, the kernel size $k = 1$ slides, transforming an m -dimensional space (representing the concatenated values of flux, centroid, and background) into a d -dimensional space at each time step t . The output of the first CNN layer is the input of a second convolution. The number of filters in the second convolution layer is set to match the model dimension d . The final embedding after the second convolution layer is expressed as:

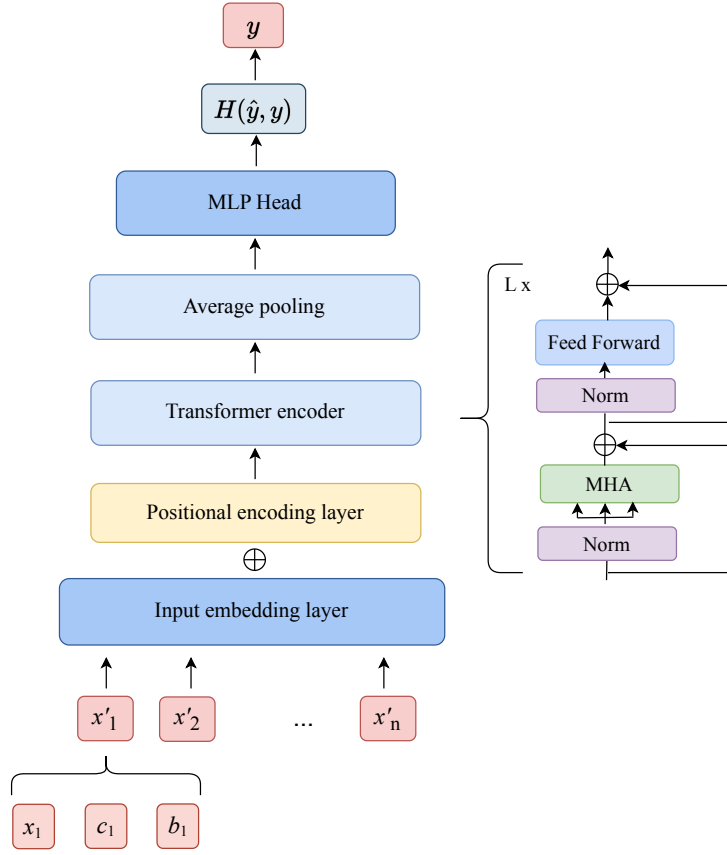


Figure 2. Schematic of the proposed architecture. The input includes flux x_i , centroid c_i , and background b_i time series, which are concatenated into input embeddings x'_i which are processed using convolutional embeddings. The tokens, along with positional encodings, are passed through a MSA mechanism within a transformer encoder. The features embedding produced by the transformer encoder are then passed through to average pooling, followed by a feed-forward MLP head to predict the class. The predicted output \hat{y} is evaluated using a loss function $H(\hat{y}, y)$ to classify the input into one of two classes (0 or 1).

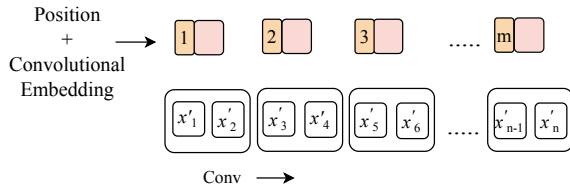


Figure 3. CNN embedding, where the kernels slide across the input time series, transforming each local window into an embedding vector.

$$\mathbf{X}_{\text{emb}} = \text{CNN}_2(\text{CNN}_1(X)) \quad (3)$$

where, $\mathbf{X}_{\text{emb}} \in \mathbb{R}^{T \times d}$ is the embedded representation, with T being the number of tokens generated after the convolution process, X represents the input features (flux, centroid, background) and d is the dimension of the output embedding space.

After the layer where we create the convolutional embedding, we combine it with the positional encoding method proposed by Vaswani et al. (2017). Positional encodings provide information about the order of the time steps; it allows the model to identify temporal dependencies and relationships in the data after the CNN layers. The positional encoding is added to the embeddings as:

$$\mathbf{Z}_0 = \mathbf{X}_{\text{emb}} + \mathbf{P} \quad (4)$$

where $\mathbf{P} \in \mathbb{R}^{T \times d}$ represents the positional encoding for each token to help the model interpret the sequential pattern, which is defined as:

$$\mathbf{P}_{(p,2i)} = \sin\left(\frac{p}{10000^{2i/d}}\right), \quad \mathbf{P}_{(p,2i+1)} = \cos\left(\frac{p}{10000^{2i/d}}\right) \quad (5)$$

where p represents the position of an element in the input sequence and i that is used for mapping to indices of the positional encoding.

4.3.2 Encoder

In this work we used the encoder inspired on transformer encoder proposed by Dosovitskiy et al. (2020) to capture global patterns and long-range dependencies within the time series light curves beyond the short-term correlations identified by the convolutional embedding. The Transformer encoder allows the model to weigh the importance of different time steps, enabling it to identify significant features relevant to exoplanet transit signals within the entire light curve, even amid the variability of the stars.

The encoder uses the self-attention mechanisms to capture the relationships between different time steps within the light curves. This self-attention mechanism assigns varying levels of importance to different points in the sequence (Vaswani et al. 2017). Thus, the model is able to focus on specific sections of the light curve, such as potential exoplanet transit signals, while disregarding irrelevant noise or variability star. The use of MSA layers facilitates the MSA mechanism in the encoder. This allows the attention mechanism, through multiple heads, to learn diverse and complementary representations of the light curve time series data, capturing different interactions and patterns that a single-head attention approach might miss. For this work, we employ $l = 4$ self-attention layers and four heads. Additional experiments with different layer configurations and their impact on performance are detailed in Section 5.2.

The embeddings are initialized combining convolutional features and positional encodings (see Equation 4). For each layer encoder l , the process is described as follow:

$$\mathbf{Z}'_l = \text{MSA}(\text{Norm}(\mathbf{Z}_{l-1})) + \mathbf{Z}_{l-1}, \quad \text{for } l = 1, \dots, L \quad (6)$$

where \mathbf{Z}_{l-1} is the input to l -th encoder layer, Norm represents layer normalization, L is the number of layers of the Transformer encoder, and MSA is the MSA operation (MSA, see Appendix A).

The layer normalization, as well as the residual connections, are integral to the encoder to contribute to the stability and efficiency of the model during training (Wang et al. 2019). These techniques help prevent issues like vanishing or exploding gradients (Ba et al. 2016). In addition, the layer ensures that the inputs to the attention mechanism are consistently scaled (Dosovitskiy et al. 2020), stabilizing the distribution of activations. Consequently, the attention mechanism focuses more effectively on different parts of the light curve data, which includes complex patterns such as stellar variability. This stabilization not only improves the ability of the model to manage and interpret these transit signals but also improves training stability and convergence speed (Wang et al. 2019).

Once the self-attention mechanism processes the input embeddings to captures contextual relationships, each time step passes through a position-wise feed-forward network, which also includes a residual connection:

$$\mathbf{Z}'_l = \text{MLP}(\text{Norm}(\mathbf{Z}'_l)) + \mathbf{Z}'_l, \quad \text{for } l = 1, \dots, L \quad (7)$$

where MLP is applied to the normalized output \mathbf{Z}'_l . This component also applies a non-linear transformation, specifically we use the Gaussian Error Linear Unit (GELU) (Hendrycks & Gimpel 2016) activation, as proposed in the encoder of (Dosovitskiy et al. 2020). GELU is known for its smoother, probabilistic non-linearity, which facilitates more stable and efficient gradient flow during training. This enables the network to model complex and non-linear relationships within the light curve. Without this non-linearity, multiple layers would collapse into a single linear transformation. As the number of layers increases, the non-linear transformations allow the network to

build progressively more complex representations (Goodfellow et al. 2016; Dosovitskiy et al. 2020).

After L stacked encoder layers, the final representation is obtained through layer normalization applied to the output of the last layer:

$$\mathbf{Y} = \text{Norm}(\mathbf{Z}_L) \quad (8)$$

At this point, \mathbf{Y} represents the normalized output of the linear encoder layer, which encodes the sequential information after the self-attention and feed-forward operations.

Finally, we apply average pooling to downsample the features (LeCun et al. 2015), defined as:

$$\mathbf{Z}_{\text{final}} = \frac{1}{T} \sum_{t=1}^T \mathbf{Z}_t \quad (9)$$

where T is the sequence length and \mathbf{Z}_t represents the output features at each time step. Each \mathbf{Z}_t is derived from the output \mathbf{Y} after the normalization layer. The downsampling operation helps the NN to reduce the number of features in the subsequent layers, allowing them to focus on more abstract and comprehensive representations of the light curves.

4.3.3 Final linear and sigmoid layer

In the final layer, the feature vector passes through a final linear transformation. This fully connected linear layer takes the encoded representation from the transformer and projects it into a logits vector, which refers to the raw, untransformed values output by the model that represents the relative likelihood of each class. For binary classification, we apply a sigmoid activation function to the output of this linear layer, which converts the logits into a probability score (Goodfellow et al. 2016). The sigmoid function ensures that the output is a value between 0 and 1, which represents the likelihood of the input belonging to the positive class, where a threshold is applied to this score to determine the final classification. The final transformation is defined as:

$$\hat{y} = \sigma(\mathbf{W} \cdot \mathbf{Z}_{\text{final}} + b) \quad (10)$$

where \hat{y} is the predicted probability score, \mathbf{W} is the weight matrix of the final layer, $\mathbf{Z}_{\text{final}}$ is the output of pooled feature vector from the encoder, and b is a bias term. The function $\sigma(x)$ represents the sigmoid activation function.

4.4 Experimental setup

Our model, detailed in this work, was developed using PyTorch Paszke et al. (2019), an open-source framework. Experiments were performed on an NVIDIA GeForce 1080 Ti with 11 GB of memory. The code is available online³.

4.4.1 Regularization & Optimizers

Dropout is a regularization technique in which a subset of neurons is randomly deactivated during the training phase to prevent overfitting (Srivastava et al. 2014). Following the approach of Vaswani et al. (2017), we applied a dropout rate of 0.1 to the output of each layer.

³ https://github.com/helemysm/FII_TransformerNN

We use the Adam optimizer, a variant of stochastic gradient descent (SGD) (Kingma & Ba 2014), because it adapts the learning rate dynamically as the network learns, which can lead to more efficient and effective training compared to using a fixed learning rate. To initialize the model, we set a relatively high learning rate of $\alpha = 0.001$, which progressively decreases as the network learns and the loss function value reduces. To implement this, we introduce a learning rate schedule, which lowers the learning rate over time (Goodfellow et al. 2016). Starting with an initial learning rate of $\alpha = 0.001$, the rate is reduced by 20% if there is no improvement in model performance after 5 to 10 epochs. This gradual decrease helps the model fine-tune its weights and improve convergence during training. In practice, this adjustment allows larger updates early in training and smaller adjustments later as the model improves its predictions (Goodfellow et al. 2016).

4.4.2 Training details

We trained our model using the labelled data sets described in Section 4.2. Our model has planet and non-planet labels (1,0) as output options. During the training, we perform the data augmentation process described in Section 4.1.2. Throughout each iteration of the training process, the model trains on diverse samples, which is made possible by the data augmentation techniques we have implemented. This ensures that the model does not see the same samples repeatedly, which helps enhance its generalization capabilities by exposing it to a variety of inputs. Additionally, during the training process, we implement the light curve injection process described in Section 4.2, which introduces new samples randomly throughout the training. We use all samples in batches of 120, which allows the model to efficiently process and learn from the data while optimizing memory usage. Each epoch consists of 400 iterations, with a duration of approximately 15 minutes. Our experiments were performed over 200 epochs, resulting in a total training time of around 30 hours.

5 EVALUATION

Our evaluation test set consists of light curves from confirmed exoplanet candidates and false positives, such as EBs, and non-transit light curves. Since targets may have been observed across multiple sectors, we ensured that none of the targets in the evaluation set have associated targets in other sectors included in the training or validation sets. This separation guarantees that the model is tested not only on unseen light curves but also on unseen targets, preserving the integrity of the evaluation process.

5.1 Performance evaluation metrics

We evaluate our model using two classes: planet (positive instances) and not planet (negative instances). As we mentioned before, most of our dataset belongs to negative instances, and due to this imbalance, accuracy is not an appropriate metric as it can introduce bias by favouring the majority class. Therefore, we evaluate the performance of our model with metrics for unbalanced datasets and for binary classification. We focused on the Area Under the Receiver Operation Characteristic Curve (AUC-ROC) score metric and F1 score (Powers 2020). The AUC score is used for binary classification, and it provides a single value to summarize the true positive rate and the false positive rate. F1 score is the harmonic mean of the precision (how many identified exoplanet transits are correct) and recall (how many real exoplanet transits were detected).

In our work, the AUC score helps us to evaluate the ability of the model to distinguish between true exoplanet transits and false positive signals like EB or non-transit signals. While the AUC score focuses on the model's overall classification performance, the F1 score provides an evaluation that considers both precision and recall. This helps us know how well the model identifies exoplanet transit while minimizing false positives and missed true transits. For each evaluation in all of the experiments, we perform 10-fold stratified cross-validation, taking the mean as the final result.

5.2 Results

Our model was evaluated with samples, which the network has not seen up to this point, which includes light curves from confirmed and known planets, EBs, and non-transit such as IS and V. This evaluation is based on metrics described in Section 5.1. In addition, since the majority of light curves are expected to have no planetary transit signals, we evaluated the generalization capability of our model across different sectors of TESS by calculating the percentage of candidates detected by our implemented models. For this evaluation, we randomly selected a sample of light curves from the SPOC dataset and made predictions to determine the percentage containing exoplanet transit signals. As a result, our model identified that approximately 0.1% of the light curves contain planetary transit signals, demonstrating its generalization ability across multiple sectors and its effectiveness in handling complex stellar variability. The main goal of this work is to improve the exoplanet candidate identification process, not only by increasing the likelihood of detecting potential candidates but also by reducing the false positive rate. This will improve the examination process for human vetting, as there will be fewer signals to analyze, with a higher probability that any given signal will contain an exoplanet. Currently, many DL approaches focus on the examination of pre-selected candidates (Valizadegan et al. 2022), as this remains a challenge in the field of exoplanet detection.

Table 2 shows the performance results for our model across various experimental configurations, including the use of centroid time series and background time series as input for our model. As a result, we found that incorporating the background time series significantly improves the performance of our model. In comparison, the centroids also contribute to performance improvement, but their impact is slightly less substantial.

Regarding the components of the attention mechanism, our default model is trained with four heads, as increasing the number of heads beyond this threshold yielded no significant improvement in performance while also leading to increased computational cost. We varied both the number of layers and the number of dimension embedding. Reducing $l = 2$ results in a 2 percent decrease in the AUC-ROC score, while setting $l = 8$ yields an AUC-ROC score equivalent to that of $l = 4$ and an F1 score with a 1 percent improvement for $l = 8$. However, we opted to use $l = 4$ as our default model as the reduced computational costs outweighed the increase in predictive performance for our use case.

Additionally, the Table 2 highlights the impact of training the model without injected light curves, providing insights into how these injections affect the overall performance. Our results showed an improvement in the AUC-ROC score, and beyond that, we also made predictions to identify new candidates within a randomly selected sample from the SPOC dataset. Consequently, the model without data injection identified that approximately 0.36% of the light curves contain planetary transit signals. This suggests that the model trained with data injection effectively reduces the number of light curves that need to be examined to determine potential planet candidates. These

Table 2. Summary of the results in terms of AUC-score and F1-score. Default model is: $l = 4$, $d_{emb} = 512$, with centroid and background time series, and with injected LCs.

Model	Avg. auc score	Avg. F1-score
Default	0.88	0.82
$l = 2$	0.84	0.80
$l = 8$	0.88	0.83
Without centroid	0.87	0.80
Without background	0.85	0.80
$d_{emb} = 128$	0.80	0.76
$d_{emb} = 256$	0.84	0.79
Without injected LCs	0.86	0.82

results suggest that training with injected data and the inclusion of background and centroid time series not only improves the performance but also allows for a more efficient evaluation of light curves.

6 SEARCHING NEW CANDIDATES

In this section, we describe the process of identifying new exoplanet candidates using our trained model. We made predictions on SPOC data from sectors 1 to 26 with the aim of discovering previously undetected exoplanet candidates. Given that these sectors have already been extensively analyzed by numerous candidate search pipelines, employing both traditional methods and machine learning approaches, many possible candidates have already been catalogued. We filtered out all candidates that were already listed in the ExoFOP catalogue, as it is considered the authoritative source for previously identified candidates.

We developed a pipeline for the identification process, beginning with the inference of light curves to extract potential candidates. Our model evaluated a total of 4.1 million light curves, identifying 0.1% with a probability of containing planetary transit signals. Among the light curves identified, both single-planet multi-transit and single-transit events were detected, each requiring a specific vetting approach. Figure 4 shows the general procedure for identifying new candidates. Once our trained model performs inference on new light curves and identifies those that contain potential planetary transits, we calculate the transit parameters for these candidates. We used various techniques for vetting the light curves identified. For detailed information on these examinations, refer to Section 6.1, Section 6.2 and Section 6.3.

6.1 Single-planet multi-transit light curve candidates

Single-planet multi-transit light curve candidates are those where multiple transit events are observed at regular intervals in the light curve, indicating a consistent orbital period around the host star. Some planetary systems may not show multiple transits due to observational time, such as long orbital periods that exceed the duration of the observations. Additionally, systems with TTVs can cause variations in the timing of transits, making them deviate from strict periodicity. The multiple transits in the light curve at regular intervals not only help confirm the presence of the exoplanet candidate but also enable more precise estimations of its orbital parameters.

To verify these candidates, we first apply the Box-Least Squares

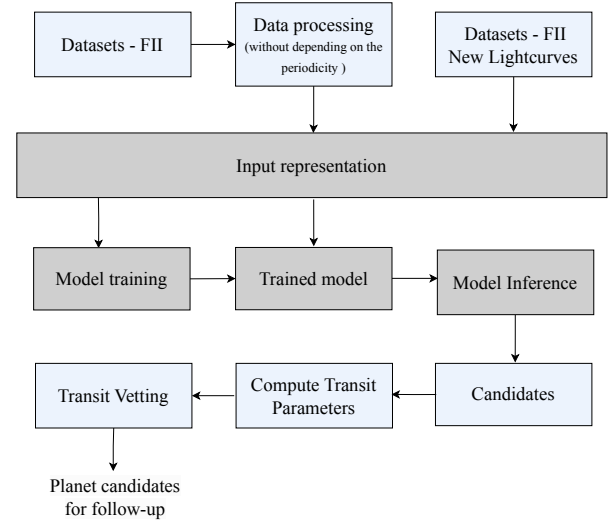


Figure 4. General diagram for the identification of new exoplanet candidates based on model predictions. The blue boxes represent the inputs to the NN and the outputs after inference (candidates and transit vetting). The grey boxes are related to the NN, which includes the creation of the input representation, used to train the model and subsequently perform inference to find candidates. After inference, the resulting candidates are evaluated through transit vetting to identify potential exoplanets for follow-up observations.

(BLS; Kovács et al. 2002) periodogram to compute the transit parameters. BLS is an algorithm designed to search for periodic signals in light curves, specifically focusing on those that have a box-shaped transit shape. After computing the transit parameters, we calculate the radius of the planet $r_p = r_* \sqrt{d(c+1)}$, using the radius of the target star r_* and the target’s background contamination c . The stellar radius r_* and the c are obtained from the TIC, accessed through the Mikulski Archive for Space Telescopes (MAST) using Astroquery package. When the stellar radius is not available in the TIC, we use the Gaia mission’s (Vallenari et al. 2023) data release 3 as a secondary source. We discard planet candidates with a predicted radius greater than $1.8R_{\text{Jupiter}}$. This threshold is set to focus on identifying planets that lie within the typical size range of gas giants and smaller exoplanets, as larger objects are more likely to be low-mass stars, brown dwarfs, or other non-planetary astrophysical phenomena (Hodžić et al. 2018; Carmichael et al. 2020). According to the BLS outputs, approximately 20% of the signals have physical parameters consistent with a planetary transit.

After using BLS, we used the Discovery and Vetting of Exoplanets (DAVE) tool, developed by Kostov et al. (2019). Only those signals that passed the initial BLS filter proceeded to this subsequent examination. DAVE evaluates the candidates by examining several factors, among them checking for secondary transit signals, evaluating changes in photometric centroid positions during and outside of the transit events, and comparing odd against even transits. The check for secondary transit signals helps identify binary star systems that might mimic planetary transits, as these typically exhibit a detectable secondary eclipse. The examination of photometric centroid shifts ensures that the detected signal is originated from the target star and not from nearby stars. In some cases, DAVE classified a TIC as a candidate in one sector but flagged it as a false positive in another. In these instances, we consider the TIC to be a false positive. Af-

ter human vetting and reviewing the output of DAVE for candidates with a positive disposition, $\sim 25\%$ of the cases correspond to valid candidates.

The results from our model predictions, after completing the vetting process, are summarized in Table 3. The table presents the candidates along with their respective transit parameters, including target magnitude (TMag), transit depth, transit epoch, orbital period, transit duration, and radius. These parameters provide a detailed overview of the characteristics of the candidate. Figure 5 shows the distribution of radii for the identified candidates measured in Jupiter radii, providing insight into the range and frequency of detected planet sizes. The majority of the candidates are concentrated within a radius range between 0.75 and 1.25 Jupiter radii, with a significant peak around 1 Jupiter radius. We did not detect any Earth-sized exoplanets or smaller candidates with radii below 0.3 Jupiter radii. Figure 9 shows that stars with radii between 0 and 1 solar radii host a large number of confirmed planets with radii between 0 and 2 Earth radii (upper x-axis), suggesting that smaller planets are more commonly found around smaller stars. In contrast, our detected candidates (blue points) are concentrated in the 0.75–1.25 Jupiter radii range and mostly around stars between 0.8 and 2 solar radii. The absence of smaller planets in our findings can be attributed to several factors. For example, smaller planets, such as those near the size of Earth, typically produce shallower transits. Traditional methods such as BLS depend heavily on periodicity and may be better to detect shallower transit signals, since it considers multiple potential periods, thereby increasing detection likelihood. Our NN still has challenges in identifying these signals, especially in the presence of noise or stellar variability. Unlike BLS, our approach does not depend on periodicity, which could explain why our NN detects smaller candidates less frequently.

We compared our exoplanet candidates with ExoFOP-TESS-confirmed planets. Figure 7 shows the relationship between TESS magnitude and transit depth for confirmed exoplanets and for our candidates, indicating that our candidates are concentrated in an intermediate region of depth and magnitude compared to the confirmed planets. The relationship between the radius of exoplanets measured in Jupiter radii and their corresponding orbital periods is illustrated in Figure 7. The majority of confirmed exoplanets have orbital periods of less than ~ 5 days, but there are also many with longer periods, showing great diversity. Among our candidates showing multi-transits, we also find some with periods shorter than 5 days, extending up to 25 days.

We identified two candidates with radii slightly exceeding the threshold of $1.8 R_{\text{Jupiter}}$. For candidates that exceed this threshold, we calculated their equilibrium temperature of the planet T_{eq} using Equation 4 from Méndez & Rivera-Valentín (2017), which is calculated from the balance between the stellar flux received from the host star and the flux absorbed by the planet (Selsis et al. 2007). For candidate TIC 385921743, we calculated an equilibrium temperature of $T_{\text{eq}} = 2449.11$ K, and a radius of $1.85 R_{\text{Jupiter}}$. The radial velocity error (RV error) obtained from Gaia is 0.91 km s^{-1} . The second candidate, TIC 275614831, has an T_{eq} of 3870.08 K, and a calculated radius of $1.82 R_{\text{Jupiter}}$, and an RV error of 1.50 km s^{-1} . Despite being slightly above the threshold, these candidates were included for further consideration due to their close proximity to the limit. The T_{eq} for both candidates are near the upper range observed for known hot Jupiters but remain within it, suggesting they could be gas giants in tight orbits around their host stars, making them interesting targets for additional follow-up observations. Moreover, the radial

velocity errors are relatively low, which suggests a reasonable level of confidence in their classification as planetary candidates.

6.2 Single-transit light curve candidates

Single transits are exoplanet candidates where only one transit has been observed in the light curve of a single TESS sector. This typically happens because TESS observes each sector for 27 days, and the orbital period of these candidates is longer than the duration of a single sector light curve. Additional transits may appear in other sectors depending on the orbital period and the timing of observations. Longer-period transiting exoplanets are particularly valuable as they enable us to measure the densities of warm and cool planets (Wang et al. 2021). They often present unique opportunities for discovery, as they can represent long-period planets that may not be detectable through traditional methods, such as BLS. Furthermore, once these transits are detected, they will require further ground-based follow-up observations to determine the orbital period and differentiate from potential astrophysical or statistical false positives (Sullivan et al. 2015). Detecting and validating these signals is more challenging compared to multi-transits, which show multiple transits within the light curve.

From the NN predictions, we perform a visual inspection and identify those that have only one transit signal corresponding to ~ 400 TIC IDs, with the remaining cases evaluated as multi-transits (see Section 6.1). We verified that the detected transit signal originates from the target star itself and not from nearby stars that could contaminate the observation. Next, we discard those TIC IDs that have an RV error $> 2 \text{ km s}^{-1}$, with the RV measurements obtained from Gaia. This criterion allows us to eliminate potential false positives resulting from measurement uncertainties in radial velocity data. This filter was consistent with the radius of the candidates, as those with an RV error $> 2 \text{ km s}^{-1}$ generally had radii larger than $1.8 R_{\text{Jupiter}}$, with the exception of TIC 438122862, which has a radius of $0.93 R_{\text{Jupiter}}$ and presents only one single transit in Sector 6. After applying these filters, we verify whether the transits were detected in sectors beyond 26 to ensure consistency across multiple observations of the same transit event. Finally, for the TIC IDs identified, we extend the review to sectors from subsequent sectors, confirming the persistence of the signals or identifying any new ones. As a result, $\sim 20\%$ passed the vetting process, leaving 82 validated as single transits.

Following our model predictions and the subsequent vetting process, we present in Table 4 a detailed list of candidates identified as single transits. The distribution of single transit candidates as a function of their radii is shown in Figure 6 where most candidates have radii between 0.5 and 1.0 Jupiter radii, with a peak around 0.75 Jupiter radii (approximately 8.5 Earth radii).

An example of a candidate identified by our NN in two different sectors is TIC 232616346. Figure 10 shows the light curves of this candidate identified in sectors 20 and 23. Both sectors show the same transit event with the same depth, which validates that the candidate is the same in both sectors. Similarly, other candidates were also detected in multiple sectors, while some were identified in only a single sector because additional transits may have occurred when TESS was not observing that sector. Figure 11 presents three additional examples of single transit candidates: TIC 233577004 in sector 14, TIC 341687821 in sector 21, and TIC 122522333 in sector 3. Each of these candidates displays a clear single transit event, with some having detections in other sectors and others identified in only one sector. These light curves show the type of signals identified by our model, suggesting that these candidates may correspond to longer-period exoplanets.

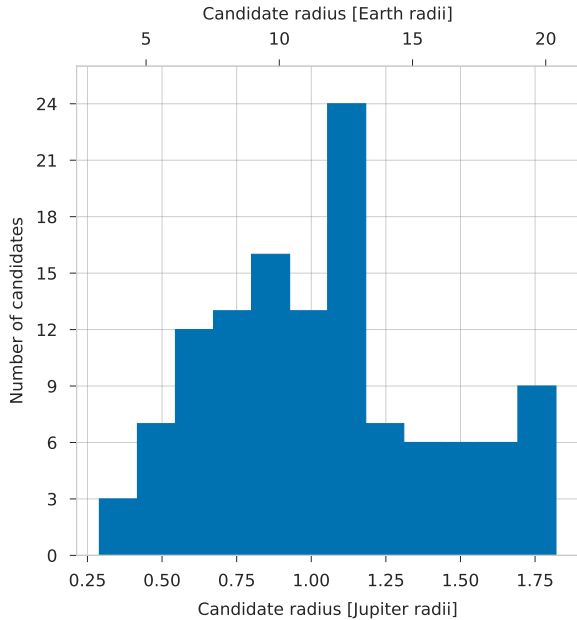


Figure 5. Distribution of single-planet multi-transit light curve candidate radii measured in Jupiter radii.

Moreover, these examples underscore the challenges in analyzing single transit events. Our model demonstrates the ability to detect the presence of a transit signal, but it is essential to perform careful validation to discard false positives and ensure the reliability of the identified candidates. In this sense, continued monitoring and follow-up observations will be crucial for confirming these candidates.

6.3 Multi-planet system candidates

Multi-planet systems are planetary systems that host more than one planet orbiting the same star. These systems usually show multiple transits with different depths in their light curves. The varying depths can be attributed to the planets of different sizes from the host star. Additionally, the orbital period of the transits differs due to the different distances of the planets from the host star.

Our NN is trained to identify transit signals in light curves, regardless of whether these signals have identical depths or orbital periods. The NN distinguishes between transit signals through the analysis of key features of the light curve, such as the shape of the dip, the variation in the brightness of the star and the timing of the signal. As a result, the NN is able to identify multi-planet systems. Among these, TIC 193096383, TIC 221567884, TIC 118798035, and TIC 400049903 were detected across sectors 1 - 26. TIC 193096383 is illustrated in Figure 14, which shows the transits of two potential exoplanet candidates, “b” (orange) and “c” (blue). To validate these candidates, we implemented an approach that combines analyses of single-planet multi-transit and single-transit light curve candidates, as detailed in sections 6.1 and 6.2. Although a detailed examination of multi-planet systems is beyond the scope of this work, we underscore the importance of further investigation of these TIC IDs.

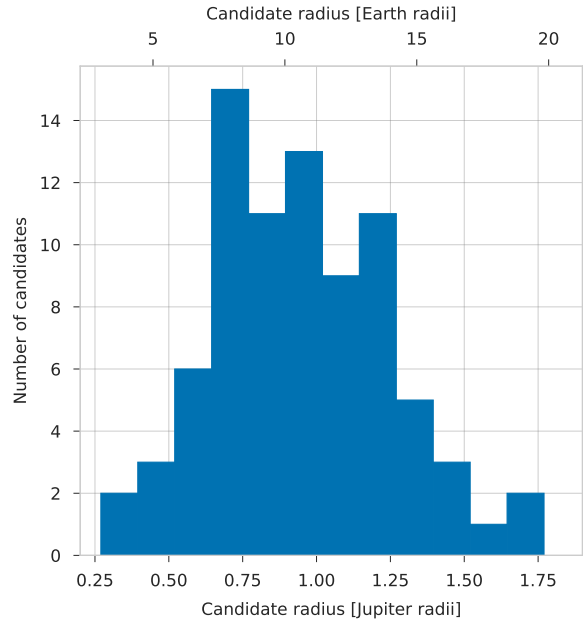


Figure 6. Distribution of single-transit light curve candidate radii, measured in Jupiter radii.

6.4 Significant candidates of special interest

As a result of this work, certain candidates emerge as particularly remarkable in the search for exoplanets due to their unique characteristics or potential for further study. We identify these candidates while noting that a more detailed analysis of them is beyond the focus of this work. We highlight the need for continued investigation and validation to uncover insights into planetary formation and system dynamics.

6.4.1 TIC 221567884

Our model initially detected TIC 221567884 as a candidate in sector 12. After further analysis using BLS, we identified two transits with different depths, suggesting it could be a multi-planet system. To discard the possibility that the TIC 221567884 belongs to an EB, we verified additional sectors > 26 for the same TIC 221567884 to ensure the consistency of the signals across multiple observations. We identified transits in sectors 39 and 66, with a particular possible mutual transit event in sector 66. In systems with more than one planet, there is a unique opportunity for photometric mutual events, where planets pass in front of or obscure each other as seen from Earth. A mutual event specifically refers to this overlap between two planets from our perspective on Earth (Ragozzine & Holman 2010). If confirmed, this mutual event would be of particular interest.

Figure 12 shows light curves for the TIC 221567884 across three different sectors from the TESS mission (sectors 12, 39, and 66). In the top panel (sector 12), there are slight flux variations with two transit events marked as “b” (green) and “c” (blue); both transit events are described in Table 5. In the middle panel (sector 39), the transit of candidate “c” (blue) is observed again, showing the same depth as in sector 12, along with the transit of candidate “d” (orange). Finally, the bottom panel (sector 66) highlights the previously mentioned mutual transit event of candidates “c” and “d”, with depths consistent with

those observed for candidate *c* in sectors 12 and 39 and for candidate *d* in sector 39. This consistency supports their identification as potential exoplanets and suggests a potential indication of planetary interactions within the system.

6.4.2 TIC 118798035

TIC 118798035 is a significant candidate within a multi-planet system, showing noteworthy TTVs. TTVs indicate deviations from the expected transit times based on a basic Keplerian model, reflecting the gravitational interactions between the planets in the system. This suggests that exoplanets in multi-planet systems often follow non-Keplerian orbits, leading to variations in the timing and duration of their transits (Agol & Fabrycky 2017).

TIC 118798035 was identified as a candidate by our model in sector 13. To further investigate this system, we extended our analysis to sectors beyond 26. In sector 39, additional transits from potential candidates were observed, providing further evidence of a multi-planet system with TTVs. Figure 13 presents the light curves for this possible multi-planet system, with the top panel showing the light curve from sector 13 and the bottom panel showing the light curve from sector 39. In sector 13, transits for candidates “b” and “c” are clearly visible. In sector 39, the transit of both candidates “b” and “c” appear again with consistent depths. Furthermore, TTVs for candidate “c” is showed in sector 39.

6.5 Analysis of false positives

Despite incorporating information on centroids and background time series to help the model learn to distinguish false positives, some false positives are still detected by our NN. An example of this is TIC 296945443 from TESS Sector 12, which was detected by our NN as an exoplanet candidate but was later identified as a false positive by DAVE. The analysis of DAVE showed a shift in the photometric centroids, which was consistent with background star contamination.

Our NN was trained on SPOC light curves, which are calculated using various photometric apertures. In the case of TIC 296945443, the aperture selected for Sector 12 did not capture the brightness variation of a nearby contaminating star, resulting in no detected centroid shift and leading to a false positive. We also examined light curves from other sectors for the same target, and in Sector 38, SPOC detected a centroid shift that confirmed the presence of a nearby object causing the transit-like signal. Our NN detected this target in Sector 38 as a candidate but with a lower probability compared to the high probability assigned in Sector 12. This analysis is consistent with the results presented in Section 5.2, demonstrating that incorporating centroid information does improve detection probability. However, it also highlights that further improvement can be made to reduce false positives. For example, one possible solution is to increase the training set, including more examples of false positives with centroid shifts. This additional data could help the model better recognize cases where background stars or centroid shifts cause false positives and, thus, improve the ability to distinguish true exoplanet candidates from false positives.

7 CONCLUSIONS

This work demonstrates the Transformer’s ability to capture long-range dependencies and focus on relevant segments of light curves, combined with a CNN embedding that effectively aids the encoder

Table 3. List of single-planet multi-transit light curve candidates.

TIC ID	Transit Epoch	Radius (Jupiter radii)	Depth (ppm)	Orbital Period (days)	Duration (hours)
123365281	1386.206	1.24	11518	2.606	2.52
88507544	1411.785	1.14	21209	2.154	1.79
245076932	1601.167	0.98	4623	21.605	4.81
32421578	1390.559	0.68	3182	4.988	2.88
138733600	1387.988	1.08	9198	3.339	2.88
302753992	1325.620	0.75	682	0.801	1.44
39017649	1332.992	1.42	8071	10.618	3.12
29756364	1325.815	0.90	5343	1.173	1.44
341497604	1325.815	1.09	2666	1.687	1.69
206584800	1355.234	0.86	2443	1.097	1.44
70514245	1387.838	1.15	19522	4.048	1.55
27986137	1389.127	1.03	10000	3.438	1.56
164695417	1387.019	0.69	3050	3.597	1.32
287203477	1386.284	1.08	2925	1.171	1.38
178215685	1411.432	0.38	908	0.618	1.36
407998915	1441.111	0.98	12663	3.132	2.16
248445793	1441.989	0.56	1114	9.621	1.81
71048340	1440.754	0.73	5200	11.617	2.64
279494608	1412.560	0.91	2040	1.793	1.22
46432937	1468.632	0.92	26522	1.440	1.17
317924729	1468.957	1.56	10367	2.002	2.88
468950016	1494.862	1.13	3207	8.910	4.82
99341082	1497.206	1.32	5683	13.262	2.88
415090780	1492.861	1.61	5127	1.747	1.80
385921743	1492.141	1.80	12760	2.336	3.12
453054952	1521.062	1.31	2469	5.238	5.04
310149582	1545.578	1.17	2875	2.756	3.12
73644471	1574.479	1.30	8180	4.591	3.84
334981118	1576.932	1.49	5322	5.587	4.79
146937007	1546.953	0.99	2837	3.048	1.23
453892431	1572.053	1.35	3136	5.132	2.16
467461269	1574.005	1.01	2158	7.776	2.76
176193144	1630.675	1.21	5408	2.708	1.56
397231954	1633.361	0.82	2428	17.318	4.79
122636751	1635.491	1.34	2406	13.691	4.79
275614831	1657.317	1.82	6212	1.140	3.48
75076259	1631.084	1.03	3025	5.968	2.88
300381700	1471.205	1.05	5163	9.072	2.41
87775884	1662.637	1.45	1716	6.874	4.56
119226450	1657.066	0.66	4632	16.747	3.82
426122272	1685.132	1.17	13968	2.942	2.88
74029268	1684.086	1.59	2748	7.909	5.76
230494128	1684.034	1.15	6043	1.344	1.22
65612701	1686.254	0.47	805	10.181	4.44
364561528	1713.814	1.17	14321	12.781	3.12
368100256	1768.194	0.64	5673	16.151	4.44
421628129	1767.682	1.13	2855	5.861	1.92
186762886	1792.961	1.51	4674	7.302	3.24
28830523	1792.464	1.72	6803	3.222	4.32
198490746	1683.758	1.18	8673	0.904	0.96
459210578	1684.746	0.67	2477	1.862	1.71
142441071	1685.515	0.93	9841	2.143	2.16
86303607	1843.545	0.82	7058	3.001	2.52
21441139	1878.852	0.92	2518	11.347	4.44
355792348	1962.123	0.81	3081	6.388	2.88
263723967	1988.135	0.68	1867	8.002	2.77
232060270	1327.161	0.73	2128	17.422	4.08
362548828	1631.901	1.52	4632	7.457	5.52
308692360	1525.015	1.13	4329	10.021	4.32
73232401	1593.009	0.36	1426	11.018	3.36
441012828	1327.212	1.67	9314	2.786	3.36
184728968	2119.861	0.90	9829	5.947	2.77

Table 3. (Continued) List of single-planet multi-transit light curve candidates.

TIC ID	Transit Epoch	Radius (Jupiter radii)	Depth (ppm)	Orbital Period (days)	Duration (hours)
328100489	1389.925	1.53	10920	4.702	4.08
305540712	1522.485	0.78	5084	15.082	2.40
365717150	1608.829	0.99	754	11.907	3.48
383829317	1689.937	1.06	2421	9.912	2.64
355206662	1874.296	0.77	7142	3.934	1.20
137020190	1901.809	0.84	6281	23.057	3.36
459801869	1933.236	1.05	3004	20.381	4.81
436255371	1703.092	0.88	2588	24.028	3.84
321011198	1388.179	0.48	4333	7.402	2.52
168790078	1416.657	0.63	1511	6.342	1.44
250133183	1442.901	1.02	4155	4.478	1.44
386518121	1524.317	0.72	6306	6.051	1.92
185980211	1521.703	0.71	1191	2.962	2.28
147566325	1548.537	1.41	1596	8.285	3.62
4809705	1549.352	0.57	1908	4.461	3.12
163029327	1574.351	0.72	5454	2.562	1.61
20614436	1574.608	0.52	2625	7.601	1.25
275548876	1634.489	0.55	881	9.053	2.16
35771052	1630.969	1.06	1819	7.059	2.76
85651189	1663.123	0.81	1898	4.081	2.88
251619073	1791.553	0.88	1531	1.578	2.52
158922455	1685.843	0.45	3671	1.633	1.86
295117707	1719.467	0.76	5393	6.881	1.92
193386434	1687.317	1.28	2628	2.868	2.76
63637169	1741.783	0.99	891	5.622	4.08
388076435	1742.662	0.29	619	2.565	1.30
73638456	1793.813	0.48	2475	2.108	2.16
428320381	1794.662	1.80	6016	2.434	4.08
273858602	1819.868	0.64	3855	1.619	1.44
350215049	1333.385	0.83	4360	9.124	4.44
152508218	1415.589	0.66	3918	9.305	2.52
117646374	1439.241	0.62	2641	1.889	1.84
138854818	1472.193	1.78	9692	5.789	4.82
150165026	1414.126	1.25	5709	7.778	1.56
32164949	1496.752	0.57	20882	8.463	2.88
463279737	1547.778	1.12	1589	4.961	2.16
410056850	1664.842	1.13	6915	10.618	4.44
229539379	1685.014	1.68	8450	9.644	4.81
391839433	1816.503	1.69	7637	2.721	3.72
193034981	1686.796	1.67	7332	3.547	3.48
425937489	1326.472	1.13	7491	15.572	1.19
38833595	1327.242	1.13	4475	12.043	1.22
314867507	1354.861	1.18	6987	2.474	1.89
343813363	1414.026	1.10	10611	5.011	3.48
439902212	1412.141	1.18	10527	22.393	4.19
407993292	1442.994	1.28	11509	5.977	1.23
187102522	1519.277	1.78	6852	2.149	3.48
146320244	1544.876	0.54	1910	4.485	2.52
137391077	1989.352	1.15	3450	9.032	4.44
341938350	2010.969	0.87	3117	14.027	3.48
258243070	1985.017	1.77	9345	7.462	4.08
339502646	1847.148	0.88	2897	15.625	3.72
39015621	1845.614	0.62	4350	6.102	3.72
87878954	1817.800	0.94	2070	2.314	3.12
242843507	1765.785	1.74	14525	19.303	4.08
373662662	1740.749	0.78	1736	6.924	2.76
64770659	1713.666	0.48	1942	4.607	3.72
230966894	1655.421	1.13	4245	2.651	1.44
253637358	1660.381	1.33	4976	3.451	2.52
193164274	1629.370	1.79	11024	4.012	3.12

Table 4. List of single-transit light curve candidates.

TIC ID	Transit Epoch	Radius (Jupiter radii)	Depth (ppm)	RV Error (km s ⁻¹)	Sector
52285162	1352.935	0.70	6540	1.231	1
89546401	1363.241	1.27	7385	1.354	2
358289302	1354.862	0.70	5365	1.664	2
199735531	1357.684	0.92	5317	1.287	2
122522333	1389.3684	0.74	1792	0.41	3
63921468	1400.3114	0.86	1256	0.419	3
100991578	1433.509	0.65	1313	0.544	4
343839315	1415.543	1.15	5771	1.692	4
9939655	1416.462	0.87	1766	0.283	4
92304420	1413.747	0.44	2832	0.322	4
283631762	1457.599	0.69	4708	0.642	5
123570723	1468.862	0.99	5688	0.41	6
438122862	1475.322	0.93	2071	2.467	6
231340540	1495.131	0.74	5172	0.908	7
149965576	1499.412	1.23	3243	0.309	7
388014300	1499.69	1.45	10440	1.6	7
455201271	1494.362	0.71	5309	0.742	7
141786309	1507.399	1.44	2300	1.006	7
434452008	1539.751	0.62	2754	0.456	8
117888314	1526.051	0.78	1083	1.152	8
19265777	1520.933	0.81	2083	0.765	8
238060327	1519.101	1.30	7427	0.95	8
334656125	1523.374	0.70	1782	0.353	8
289596640	1539.431	0.91	2168	0.247	8
106056929	1548.591	0.83	5170	1.138	9
36541001	1566.125	1.25	4253	0.779	9
147027702	1550.517	1.21	3022	0.331	9
105712339	1561.807	0.89	6512	1.212	9
40561422	1593.072	1.12	2848	0.904	10
97975310	1577.598	1.09	4686	0.433	10
57533297	1590.158	0.93	7343	1.382	10
266376971	1586.723	0.30	778	0.183	10
394354824	1620.739	1.67	6138	1.616	11
449486364	1642.242	1.35	5876	0.966	12
247934029	1646.182	0.42	1169	-	12
182456927	1670.689	1.03	5352	0.879	13
265371495	1659.879	0.92	7616	1.418	13
29778074	1660.486	0.75	3384	1.423	13
42196078	1697.922	0.85	3002	0.287	14
210175389	1690.582	1.77	15190	1.47	14
48304182	1688.822	1.35	6803	1.114	14
266908297	1686.922	0.71	5533	2.660	14
147898114	1698.252	1.06	9752	1.477	14
233577004	1704.192	1.16	5721	0.354	14
269130683	1698.191	1.06	4149	0.931	14
341687821	1692.988	0.56	1752	0.315	14
194125303	1705.256	0.27	988	0.204	14
224299778	1727.366	0.88	1947	0.3	15
282926264	1731.746	1.52	7931	1.27	15
219466517	1731.474	0.97	1937	0.226	15
256783400	1733.189	0.97	3983	1.251	15
429219512	1730.989	1.44	5455	1.336	15
288160753	1730.683	0.91	11791	1.939	15
99919551	1719.081	0.68	8121	1.089	15
174307526	1757.823	0.60	18868	1.822	16
162033431	1743.642	0.61	3361	0.575	16
412119944	1779.572	0.99	3902	0.783	17
85254937	1785.362	0.99	3813	0.664	17
440675630	1766.572	0.85	5585	0.724	17
241134937	1796.731	1.01	4899	0.25	18

Table 4. (Continued) List of single-transit light curve candidates.

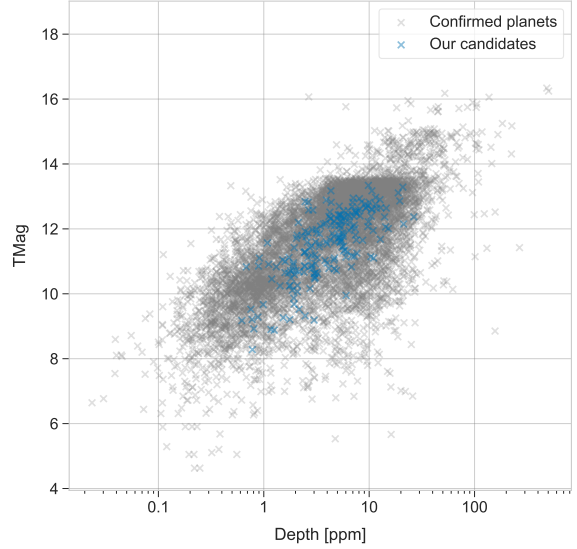
TIC ID	Transit Epoch	Radius (Jupiter radii)	Depth (ppm)	RV Error (km s ⁻¹)	Sector
397986100	1799.102	1.10	7548	0.765	18
326808653	1810.721	1.12	2085	-	18
402848417	1829.641	1.21	5988	1.452	19
82011491	1830.911	0.48	773	0.179	19
233096001	1823.721	0.72	5507	1.261	19
273856464	1822.941	0.82	3080	0.86	19
252895642	1853.361	0.68	1927	0.251	20
232616346	1853.731	1.26	4006	0.428	20
68380016	1848.051	1.13	2019	-	20
229702978	1874.501	1.21	5275	1.429	21
302728777	1877.541	0.91	4267	0.842	21
85334736	1906.357	0.71	3180	0.313	22
144314863	1906.027	0.62	2460	0.446	22
115861501	1919.057	0.53	3378	0.812	22
207363637	1922.867	0.74	10753	1.38	22
458457997	1938.378	1.15	12857	1.998	23
416023266	1937.798	1.06	4697	1.036	23
135221230	1936.528	0.82	6452	0.505	23
41743658	1960.408	0.98	2469	0.148	24
18632388	2005.602	1.21	3035	-	25
357597620	1993.972	1.25	7207	1.462	25
275267824	2020.552	1.36	7222	0.405	26

Table 5. List of candidates identified as multi-planet system.

TIC ID	TessMag	Transit Epoch	Depth (ppm)	Radius (Jupiter radii)
TIC 193096383 (b)	12.23	1546.82	2870	0.57
TIC 193096383 (c)	12.23	1559.01	9564	1.04
TIC 221567884 (b)	9.09	1629.92	868	0.48
TIC 221567884 (c)	9.09	1648.66	2169	0.75
TIC 221567884 (d)	9.09	2372.65	3037	0.91
TIC 118798035 (b)	11.29	1656.35	5970	0.86
TIC 118798035 (c)	11.29	1663.91	10660	1.16
TIC 400049903 (b)	11.61	1669.72	4041	0.61
TIC 400049903 (c)	11.61	1778.60	2424	0.47

in learning short-range patterns and variations. This combination allows for the detection of both multi-transit and single-transit light curves without prior transit parameters. Moreover, incorporating background and centroid time series data significantly enhanced the performance of our model, allowing it to better represent variations in the light curves, including stellar variability and instrumental effects. Although the use of Transformers in exoplanet detection, and in astronomy in general, is still in its early stages, the success of this approach suggests that Transformers could offer a valuable alternative to traditional methods.

Based on our findings, our proposed model learned the signal of an exoplanet transit independently of its periodicity, allowing it to identify transit events even in the absence of regular repeating patterns. This ability to generalize beyond periodic signals is particularly important for detecting single transits, where only one transit event is


Figure 7. Relationship between TESS magnitude and transit depth. Each point represents a confirmed planet from ExoFOP-TESS or our candidates.

observed due to long orbital periods. However, through our analysis, we found that our model did not identify any Earth-sized or super-Earth candidates. Instead, it successfully detected exoplanets with radii greater than 0.25 Jupiter radii. The Earth-sized and super-Earth planets typically produce shallower transits, which makes their detection more reliant on periodicity. In these cases, the recurring transit events allow traditional period-searching algorithms, such as BLS, to identify the smaller, more subtle signals that our model may not yet effectively detect. In addition to detecting multi-transit light curve candidates with radii greater than 0.25 Jupiter radii, our model also effectively identified single transits and multi-planet systems. In total, we identified 214 planetary system candidates, which include 122 single-planet multi-transit light curve candidates, 88 single-transit candidates and 4 associated with multi-planet systems.

As a result, the strength of our NN is that it is able to detect exoplanet transit signals within light curves without relying on their periodicity. This is achieved through training the NN to recognize the distinctive shape of the planetary transit signals, even in the presence of stellar variability. While the detection of smaller, less prominent planets remains a challenge, the success in identifying long-period candidates and complex systems underscores the potential of Transformer-based models in expanding the scope of exoplanet detection. In particular, our model operates without the need for prior transit parameters or phase folding, which are typically required by the previous approach of DL, enabling a more direct analysis of the data. This capability allows for the identification of diverse transit signals that may be overlooked by conventional techniques.

Our future work aims to analyze data from TESS sectors > 26 to identify new candidates. Additionally, we plan to improve our detection models to achieve more accurate identification of smaller exoplanets, such as Earth-sized and super-Earth candidates, while maintaining our capability to detect transits regardless of their periodicity to detect multi-planet systems or single transits. We also consider

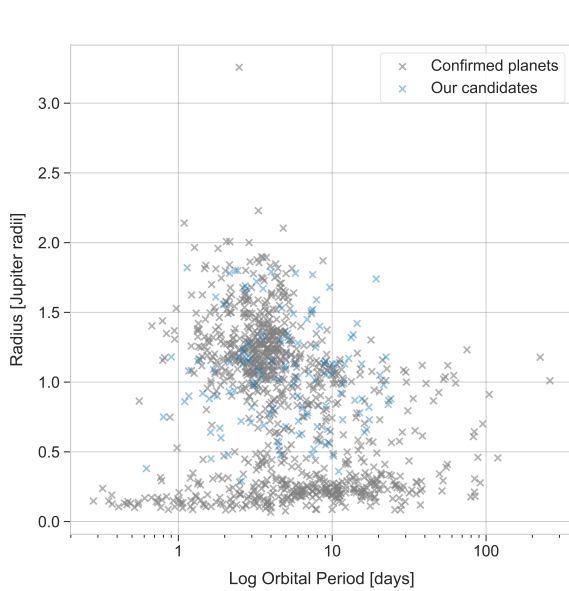


Figure 8. Relationship between radius and log orbital period. Each point represents a confirmed planet from ExoFOP-TESS or our candidates.

that upcoming missions, such as PLATO (Rauer et al. 2016) and the Nancy Grace Roman Space Telescope Roman, will present new challenges in the exoplanet search. The Roman mission, in particular, is predicted to discover between $\sim 60,000$ and $\sim 200,000$ transiting planets (Wilson et al. 2023). The approach we proposed provides a base for the development of new architectures.

ACKNOWLEDGEMENTS

The authors would like to acknowledge the support from the National Agency for Research and Development (ANID), through the FONDECYT Regular project number 1180054. HS acknowledges support from ANID, through Scholarship Program/Doctorado Nacional/2020-21212185. R.B. acknowledges support from FONDECYT Project 1241963 and from ANID – Millennium Science Initiative – ICN12_009. GO’s work is supported by NASA under award number 80GSFC21M0002. SIS’s research was supported by an appointment to the NASA Postdoctoral Program at the NASA Goddard Space Flight Center, administered by Oak Ridge Associated Universities under contract with NASA. This paper utilizes public information of the TESS mission. Funding for the TESS mission is provided by the NASA Explorer Program. Finally, thanks to the availability of data from TESS, we were able to examine and display our analysis of transit signals.

This research has made use of the Exoplanet Follow-up Observation Program (ExoFOP; DOI: 10.26134/ExoFOP5) website, which is operated by the California Institute of Technology, under contract with the National Aeronautics and Space Administration under the Exoplanet Exploration Program.

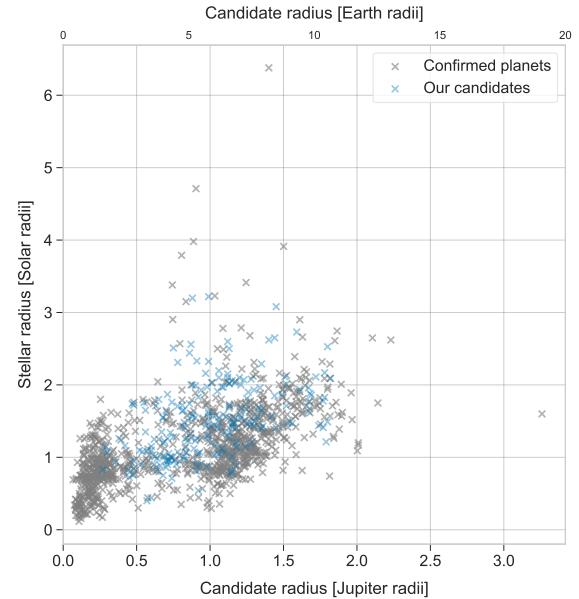


Figure 9. Relationship between radius candidate and stellar radius. Each point represents a confirmed planet from ExoFOP-TESS or our candidates.

DATA AVAILABILITY

All the data referenced here and that was used is public information about the TESS mission from Mikulski Archive for Space Telescopes (MAST), as well as data from the European Space Agency (ESA) mission Gaia.

REFERENCES

- Agol E., Fabrycky D., 2017, arXiv preprint arXiv:1706.09849
Allam Jr T., McEwen J. D., 2021, arXiv preprint arXiv:2105.06178
Ba J., Hinton G. E., Mnih V., Leibo J. Z., Ionescu C., 2016, *Advances in neural information processing systems*, 29
Bahdanau D., Cho K., Bengio Y., 2014, arXiv preprint arXiv:1409.0473
Battley M. P., et al., 2024, *A&A*, **686**, A230
Borucki W. J., et al., 2010, *Science*, 327, 977
Brahm R., et al., 2023, *AJ*, **165**, 227
Bryson S. T., et al., 2020, *Kepler Science Document KSCI-19081-003*, p. 3
Caldwell D. A., et al., 2020, *Research Notes of the AAS*, 4, 201
Carmichael T. W., et al., 2020, *The Astronomical Journal*, 160, 53
Cho K., Van Merriënboer B., Gulcehre C., Bahdanau D., Bougares F., Schwenk H., Bengio Y., 2014, arXiv preprint arXiv:1406.1078
Ciregan D., Meier U., Schmidhuber J., 2012, in *2012 IEEE conference on computer vision and pattern recognition*. pp 3642–3649
Cui K., Liu J., Feng F., Liu J., 2021, *The Astronomical Journal*, 163, 23
Dawson R. I., Johnson J. A., 2018, *ARA&A*, **56**, 175
Dawson R. I., et al., 2021, *AJ*, **161**, 161
Dosovitskiy A., et al., 2020, arXiv preprint arXiv:2010.11929
Foreman-Mackey D., Morton T. D., Hogg D. W., Agol E., Schölkopf B., 2016, *The Astronomical Journal*, 152, 206
Gehring J., Auli M., Grangier D., Yarats D., Dauphin Y. N., 2017, in *International Conference on Machine Learning*. pp 1243–1252
Gill S., et al., 2020a, *Monthly Notices of the Royal Astronomical Society*, 491, 1548
Gill S., et al., 2020b, *The Astrophysical Journal Letters*, 898, L11
Gill S., et al., 2020c, *ApJ*, **898**, L11

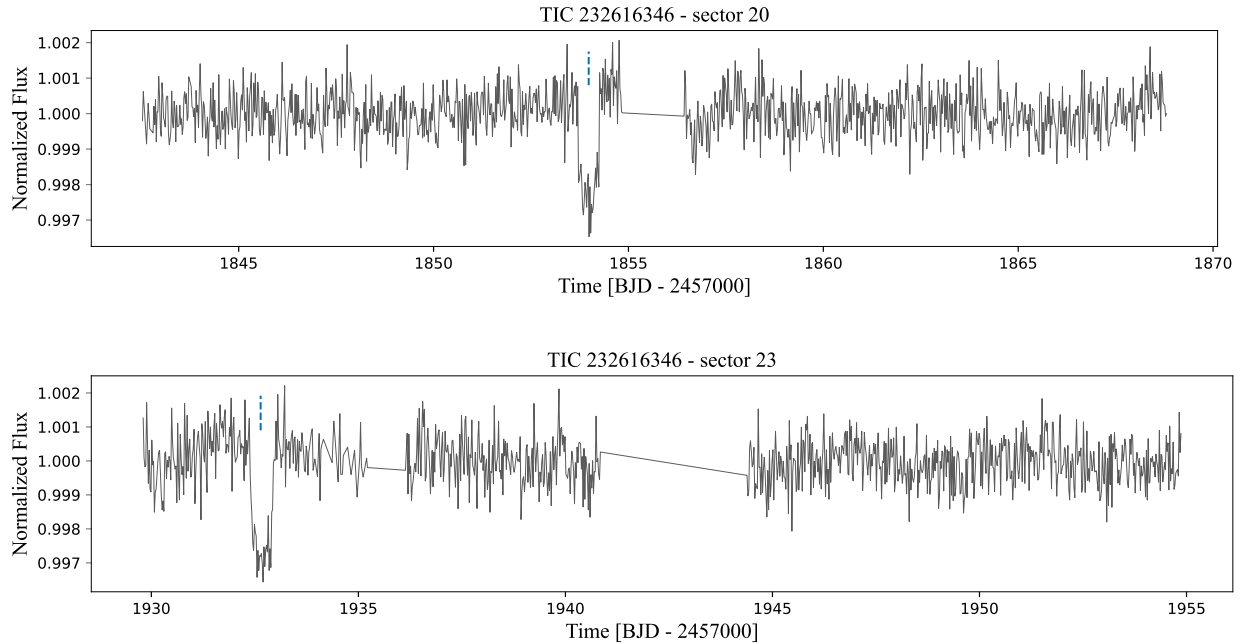


Figure 10. Light curves for TIC 232616346 in sectors 20 and 23, showing the same transit event with consistent depth, validating the detection of the same candidate in both sectors.

- Goodfellow I., Bengio Y., Courville A., 2016, Deep learning. MIT press
- Grievens N., et al., 2022, *A&A*, **668**, A29
- Guerrero N. M., et al., 2021, The Astrophysical Journal Supplement Series, 254, 39
- Hartman J. D., et al., 2019, *AJ*, **157**, 55
- Hawkins D. M., 2004, Journal of chemical information and computer sciences, 44, 1
- Hawthorn F., et al., 2024, Monthly Notices of the Royal Astronomical Society, 528, 1841
- He K., Zhang X., Ren S., Sun J., 2016, in Proceedings of the IEEE conference on computer vision and pattern recognition. pp 770–778
- Hendrycks D., Gimpel K., 2016, arXiv preprint arXiv:1606.08415
- Hodžić V., et al., 2018, Monthly Notices of the Royal Astronomical Society, 481, 5091
- Karita S., et al., 2019, in 2019 IEEE Automatic Speech Recognition and Understanding Workshop (ASRU). pp 449–456
- Kingma D. P., Ba J., 2014, arXiv preprint arXiv:1412.6980
- Kostov V. B., et al., 2019, The Astronomical Journal, 157, 124
- Kovács G., Zucker S., Mazeh T., 2002, Astronomy & Astrophysics, 391, 369
- Krizhevsky A., Sutskever I., Hinton G. E., 2012, Advances in neural information processing systems, 25
- Krizhevsky A., Sutskever I., Hinton G. E., 2017, Communications of the ACM, 60, 84
- Lakew S. M., Cettolo M., Federico M., 2018, arXiv preprint arXiv:1806.06957
- LeCun Y., Bengio Y., Hinton G., 2015, nature, 521, 436
- Lendl M., et al., 2020, Monthly Notices of the Royal Astronomical Society, 492, 1761
- Magliano C., et al., 2023, Monthly Notices of the Royal Astronomical Society, 521, 3749
- Méndez A., Rivera-Valentín E. G., 2017, The Astrophysical Journal Letters, 837, L1
- Morvan M., Nikolaou N., Yip K. H., Waldmann I., 2022, arXiv preprint arXiv:2207.02777
- Olmschen G., et al., 2021, The Astronomical Journal, 161, 273
- Osborn H. P., et al., 2020, Astronomy & Astrophysics, 633, A53
- Paszke A., et al., 2019, Advances in neural information processing systems, 32
- Pollack J. B., Hubickyj O., Bodenheimer P., Lissauer J. J., Podolak M., Greenzweig Y., 1996, *Icarus*, **124**, 62
- Powers D. M., 2020, arXiv preprint arXiv:2010.16061
- Prša A., et al., 2022, The Astrophysical Journal Supplement Series, 258, 16
- Ragozzine D., Holman M. J., 2010, arXiv preprint arXiv:1006.3727
- Rao S., Mahabal A., Rao N., Raghavendra C., 2021, Monthly Notices of the Royal Astronomical Society, 502, 2845
- Rauer H., Aerts C., Cabrera J., Team P., et al., 2016, Astronomische Nachrichten, 337, 961
- Redmon J., Farhadi A., 2018, YOLOv3: An Incremental Improvement (arXiv:1804.02767), <https://arxiv.org/abs/1804.02767>
- Ricker G. R., et al., 2014, Journal of Astronomical Telescopes, Instruments, and Systems, 1, 014003
- Ricker G. R., et al., 2015, *Journal of Astronomical Telescopes, Instruments, and Systems*, **1**, 014003
- Salinas H., Pichara K., Brahm R., Pérez-Galarce F., Mery D., 2023, Monthly Notices of the Royal Astronomical Society, 522, 3201
- Selsis F., Kasting J. F., Levrard B., Paillet J., Ribas I., Delfosse X., 2007, Astronomy & Astrophysics, 476, 1373
- Shorten C., Khoshgoftaar T. M., 2019, Journal of big data, 6, 1
- Srivastava N., Hinton G., Krizhevsky A., Sutskever I., Salakhutdinov R., 2014, The journal of machine learning research, 15, 1929
- Sullivan P. W., et al., 2015, The Astrophysical Journal, 809, 77
- Tenenbaum P., et al., 2012, *ApJS*, **199**, 24
- Tey E., et al., 2023, The Astronomical Journal, 165, 95
- Valizadegan H., et al., 2022, The Astrophysical Journal, 926, 120
- Vallenari A., et al., 2023, Astronomy & Astrophysics, 674, A1
- Vaswani A., Shazeer N., Parmar N., Uszkoreit J., Jones L., Gomez A. N., Kaiser Ł., Polosukhin I., 2017, in Advances in neural information processing systems. pp 5998–6008
- Voulodimos A., Doulamis N., Doulamis A., Protopapadakis E., 2018, Computational intelligence and neuroscience, 2018

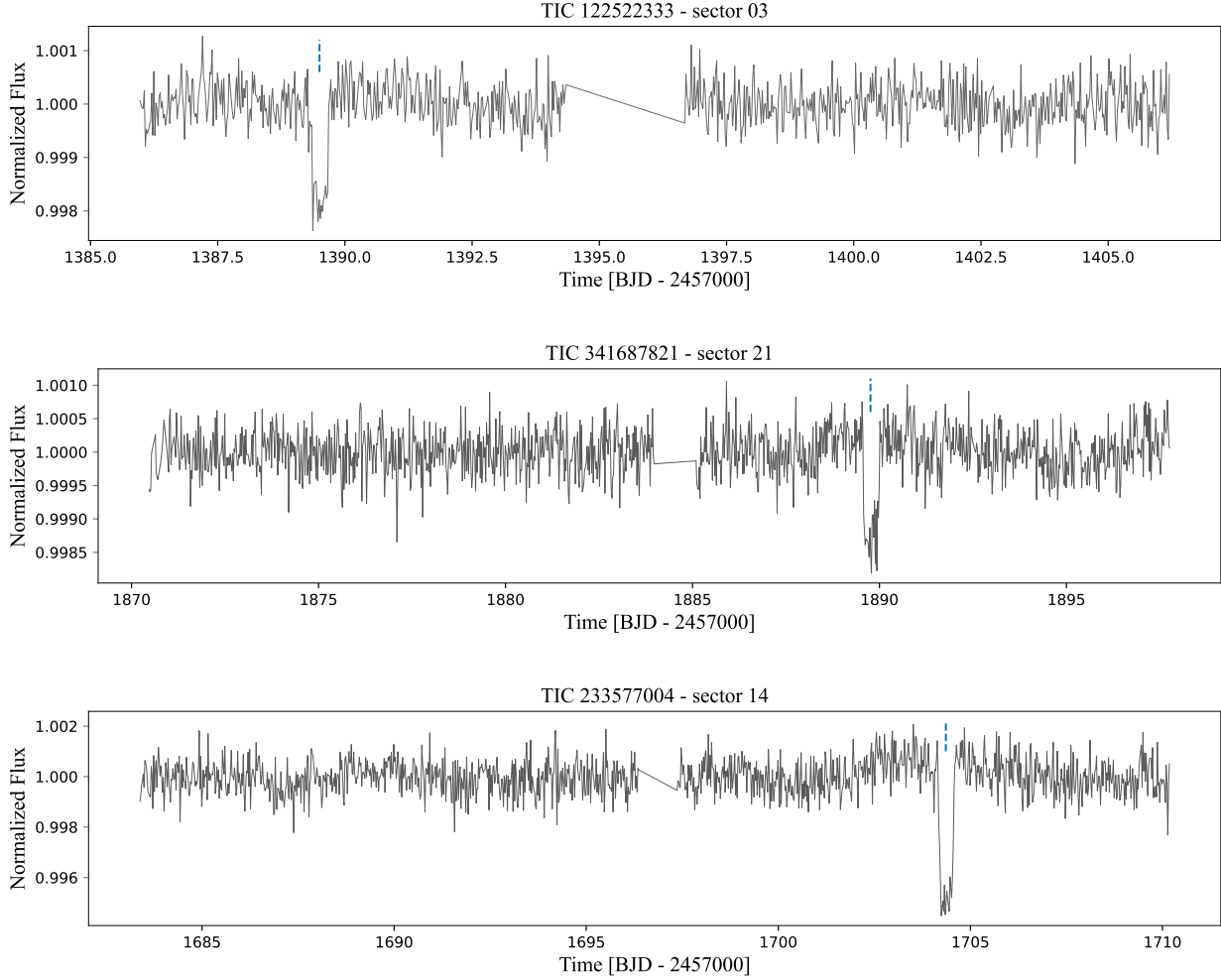


Figure 11. Three examples of single transits from TESS observations for TIC 122522333, TIC 341687821 and TIC 233577004. Each candidate shows a single-transit event in the respective sector. While these candidates were also detected in other sectors (TIC 122522333 in sector 4, TIC 341687821 in sector 14, and TIC 233577004 in sectors 21), the figure shows only the transit events from the sectors presented.

Wang Q., Li B., Xiao T., Zhu J., Li C., Wong D. F., Chao L. S., 2019, arXiv preprint arXiv:1906.01787

Wang S., et al., 2021, *The Astronomical Journal*, 162, 50

Wilson R. F., et al., 2023, *The Astrophysical Journal Supplement Series*, 269, 5

Yu L., et al., 2019, *The Astronomical Journal*, 158, 25

Zerveas G., Jayaraman S., Patel D., Bhamidipaty A., Eickhoff C., 2021, in *Proceedings of the 27th ACM SIGKDD Conference on Knowledge Discovery & Data Mining*. pp 2114–2124

Given an input sequence of embeddings \mathbf{Z}_{l-1} where T is the sequence length and d is the dimensionality of the embeddings, the self-attention mechanism computes a set of attention scores. It is computed using three vectors, the queries \mathbf{Q} , keys \mathbf{K} , and values \mathbf{V} . Vectors \mathbf{Q} and \mathbf{K} are compared to calculate similarities and obtain scores/weights for vector \mathbf{V} . To compute these vectors as three different subspace representations, the input embeddings is projected with learned weight matrices defined as:

$$\begin{aligned} \mathbf{Q} &= \mathbf{Z}_{l-1} \mathbf{W}^Q \in \mathbb{R}^{n \times d_q}, \\ \mathbf{K} &= \mathbf{Z}_{l-1} \mathbf{W}^K \in \mathbb{R}^{n \times d_k}, \\ \mathbf{V} &= \mathbf{Z}_{l-1} \mathbf{W}^V \in \mathbb{R}^{n \times d_v}. \end{aligned} \tag{A1}$$

where \mathbf{W}^Q , \mathbf{W}^K , \mathbf{W}^V are the learned weight matrices, and their dimensionalities are $d \times d_k$, with d_k represents the dimensions of the queries and keys.

Next, we calculate the attention scores using the scaled dot-product, self-attention matrix $\mathbf{A} \in \mathbb{R}^{n \times d_v}$ can be expressed as:

APPENDIX A: MULTI-HEAD SELF-ATTENTION

In this section, we describe the Multi-Head Self-Attention (MSA) mechanism used in the encoder.

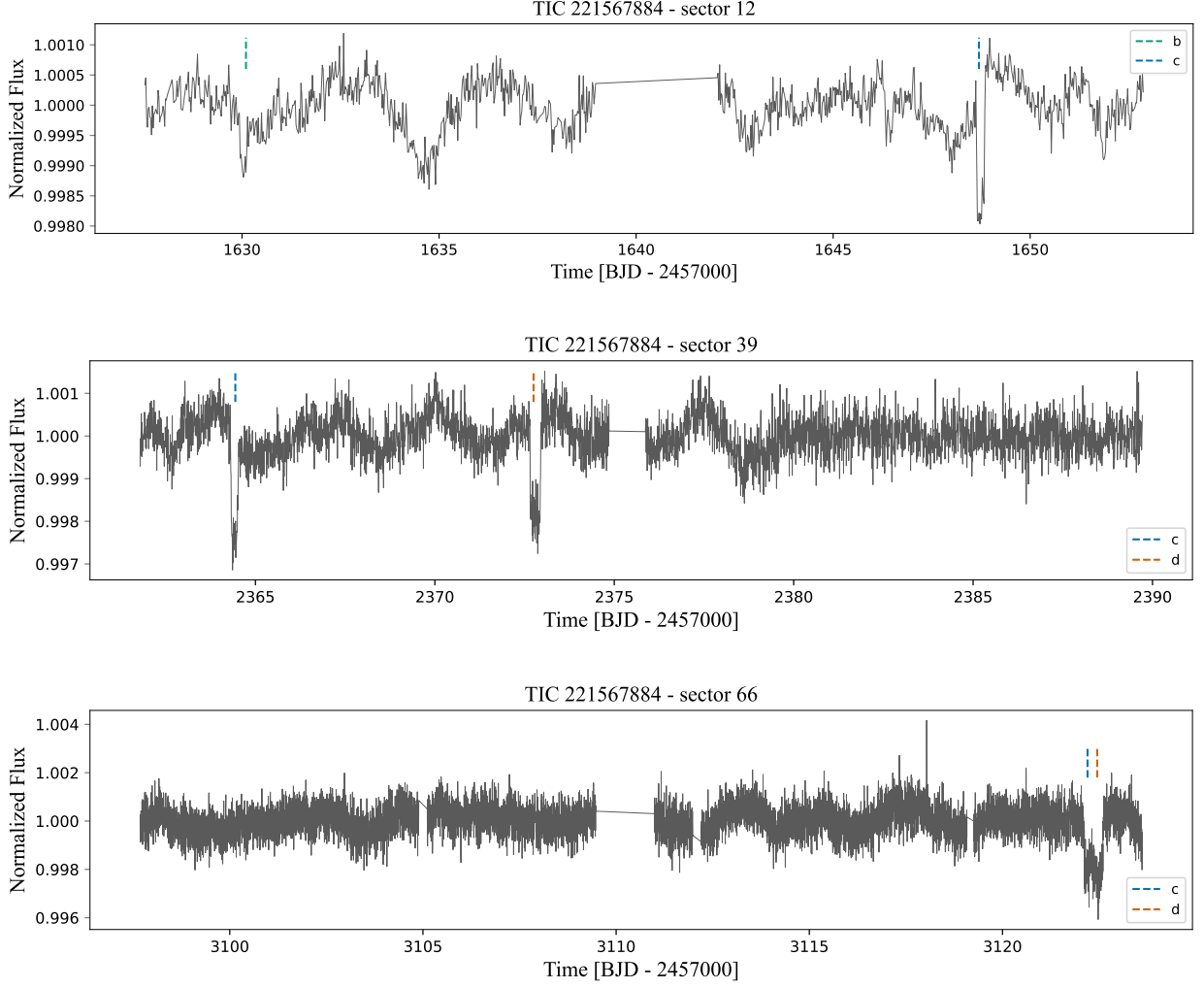


Figure 12. Lightcurves for TIC 221567884 across sectors 12, 39, and 66, illustrating transit events “b”, “c” and “d”, and a potential mutual transit event between candidates “c” and “d” in sector 66.

$$\mathbf{A} = \text{Attention}(\mathbf{Q}, \mathbf{K}, \mathbf{V}) = \text{softmax}\left(\frac{\mathbf{Q}\mathbf{K}^T}{\sqrt{d_k}}\right)\mathbf{V} \quad (\text{A2})$$

The attention layer takes the input in the form of those three parameters: queries \mathbf{Q} , keys \mathbf{K} and values \mathbf{V} . These three parameters have similar structure, where each element in the sequence is represented by a vector. The query, key, and value vectors are derived from the input embeddings and they are linearly projected h times, allowing their computations to be repeated multiple times in parallel (Vaswani et al. 2017). The outputs of these individual heads are concatenated and passed through a linear projection to create the final output defined by:

$$\text{MSA}(\mathbf{Z}_{l-1}) = \text{MultiHead}(\mathbf{Q}, \mathbf{K}, \mathbf{V}) = \mathbf{W}^O \begin{bmatrix} h_1 \\ \cdot \\ \cdot \\ h_h \end{bmatrix} \quad (\text{A3})$$

with learned output weights $\mathbf{W}^O \in \mathbb{R}^{hd_v \times d}$, and each attention head h_i computes the attention as follows:

$$h_i = \text{Attention}(\mathbf{Q}_i, \mathbf{K}_i, \mathbf{V}_i) \quad (\text{A4})$$

The resulting multi-head attention output is then passed through a residual connection and layer normalization:

$$\mathbf{Z}'_l = \text{MSA}(\text{Norm}(\mathbf{Z}_{l-1})) + \mathbf{Z}_{l-1}, \quad \text{for } l = 1, \dots, L \quad (\text{A5})$$

This paper has been typeset from a $\text{\TeX}/\text{\LaTeX}$ file prepared by the author.

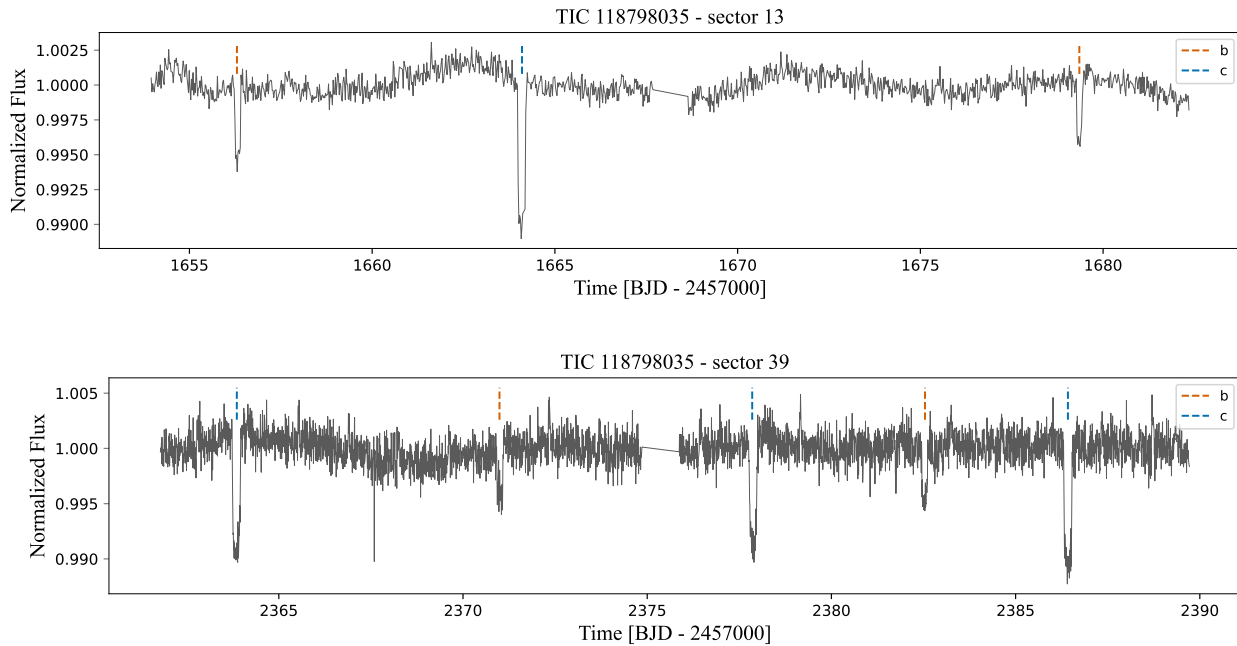


Figure 13. Light curves for TIC 118798035 illustrating a system with two exoplanet candidates. In sector 13, transit signals for candidates “b” (orange line) and “c” (blue line) are detected. The depths are consistent across both sectors, with TTVs for candidate “c” in sector 39.

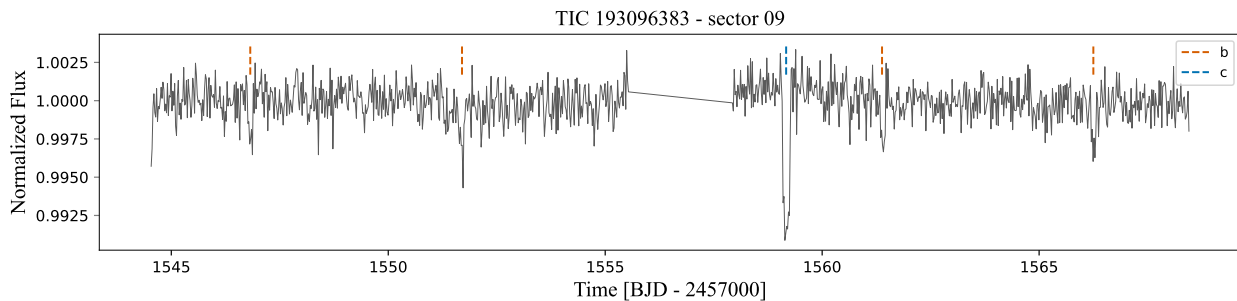


Figure 14. Light curve for TIC 193096383 in sector 9, showing the transits of candidates b (orange) and c (blue). The transits of candidate b have the same depth, which differs from the depth observed in the transit of candidate c, suggesting a potential multi-planet system.